Near-Field Optical Study of Metal-Insulator Transition in NdNiO3

Bercher, Adrien

UNIVERSITÉ DE GENÈVE
Département de Physique
de la Matière Quantique

FACULTÉ DES SCIENCES
Docteur
Alexey Kuzmenko

Near-Field Optical Study of Metal-Insulator Transition in $NdNiO_3$

THÈSE

présentée à la Faculté des Sciences de l'Université de Genève
pour obtenir le grade de docteur ès Sciences, mention Physique

par

Adrien Bercher
de
Genève (GE)

Thèse n° 5930

GENÈVE
2025

UNIVERSITÉ
DE GENÈVE
FACULTÉ DES SCIENCES

DOCTORAT ÈS SCIENCES, MENTION PHYSIQUE

Thèse de Monsieur Adrien BERCHER

intitulée :

«Near-Field Optical Study of Metal-Insulator Transition in NdNiO3»

La Faculté des sciences, sur le préavis de

Monsieur A. KUZMENKO, docteur et directeur de thèse
Département de physique de la matière quantique

Madame P. PARUCH, professeure associée
Département de physique de la matière quantique

Monsieur A. NIKITIN, professeur
Basque Foundation for Science, Bilbao, Espagne

autorise l'impression de la présente thèse, sans exprimer d'opinion sur les propositions qui y sont énoncées.

Genève, le 16 juillet 2025

Thèse - 5930 -

La Doyenne

N.B. - La thèse doit porter la déclaration précédente et remplir les conditions énumérées dans les "Informations relatives aux thèses de doctorat à l'Université de Genève".

"This page intentionally left blank"

Résumé

La transition isolant-métal dans le nickelate de terres rares $NdNiO_3$ (NNO) est un phénomène d'un intérêt majeur en physique de la matière condensée en raison de son interaction complexe entre propriétés électroniques, structurales et magnétiques. $NdNiO_3$ appartient à la classe des oxydes de pérovskite, qui présentent des transitions de phase complexes, ajustables par des paramètres externes tels que la température, la pression et le dopage. Soumis à des variations de température ou à des stimuli externes, il subit une transition rapide vers un état métallique, ce qui en fait un système idéal pour explorer les mécanismes à l'origine de la transition de phase. Notre étude examinera la dépendance de la transition en température dans des couches minces de NNO, sous une contrainte épitaxiale constante provenant du substrat : l'aluminate de lanthane ($LaAlO_3$ ou LAO).

La technique de mesure principalement utilisée pour cette recherche est la microscopie optique à balayage en champ proche par diffusion (s-SNOM). Le SNOM est une technique avancée qui combine la résolution spatiale de la microscopie à force atomique (AFM) avec la sensibilité optique d'un microscopie optique. Cette méthode performante permet d'étudier les propriétés des matériaux à l'échelle nanométrique, révélant des comportements optiques et électromagnétiques inaccessibles à la microscopie à champ lointain traditionnelle en raison de la limite de diffraction. Le SNOM fonctionne en balayant la surface d'un échantillon avec une pointe AFM tout en mesurant simultanément la lumière diffusée par l'interaction de la pointe avec les propriétés optiques locales de l'échantillon. Cela permet de cartographier les caractéristiques nanoscopiques de la topographie et des réponses optiques, telles que les polaritons des plasmons de surface, les modes de phonons et les contrastes de matériaux.

Le principal avantage de la s-SNOM est sa capacité à atteindre une résolution spatiale en dessous de la longueur d'onde utilisée, généralement jusqu'à 10 nm, tout en sondant la réponse électromagnétique locale dans les régions infrarouge et visible. Cela rend le s-SNOM particulièrement précieux pour l'étude des matériaux nanométriques, des nanostructures et de phénomènes tels que les propriétés diélectriques locales, les effets quantiques et, dans notre cas, les transitions de phase inhomogènes. Grâce à sa haute résolution spatiale et spectrale, le SNOM s'est imposé comme un outil indispensable dans des domaines allant de la nanophotonique à la science des matériaux, fournissant des informations cruciales pour la recherche fondamentale et appliquée en nanotechnologie et en physique de la matière condensée.

Le premier chapitre presente la famille des nickelates, dont le NNO fait partie. Les membres de cette famille se distinguent par les differents rayons atomiques de leur terre rare, affectant la structure cristalline et électronique du materiau. L'effet de la substitution de la terre rare montre un fort lien entre les propriétés structurelles et électroniques et indique la capacité de contrôler l'une de ces propriétés par le biais de l'autre. Dans notre cas, ce contrôle sera fait par l'intermédiaire de la déformation épitaxiale induite par le substrat, l'aluminate de lanthane ($LaAlO_3$ ou LAO), sur la couche fine de NNO.

Le deuxieme chapitre est une courte présentation du modèle de Ginzburg-Landau. Nous utiliserons ce modèle pour décrire la transition métal-isolant qui est le centre de cette recherche.

Le troisième chapitre détaille la principale technique de mesure employée dans cette étude: le SNOM. Cette méthode offre de nombreux avantages, notamment une résolution spatiale supérieure à la limite de diffraction, permettant l'étude des réponses locales et non locales de l'échantillon. Cependant, pour différencier efficacement ces réponses locales et non locales, cette approche expérimentale doit s'appuyer sur des modèles théoriques robustes et des simulations appropriées. Ces modèles, tels que le modèle du dipôle ponctuel, qui approxime l'interaction pointe-échantillon comme un dipôle induit par le champ incident, fournissent des cadres essentiels pour l'interprétation des images SNOM. En simulant l'interaction complexe des champs électromagnétiques à l'échelle nanométrique, ces approches améliorent notre compréhension des mécanismes de contraste et des propriétés des matériaux révélés par les données de microscopie.

Le chapitre quatre commence par la caractérisation de la couche mince par des mesures de rayons X, de conductivité et de réflectivité. Le chapitre se poursuit par des mesures SNOM lors de la transition métal-isolant révélant une dichotomie entre la transition durant le refroidissement et le réchauffement. Ce chapitre met en lumière la sensibilité de la métallicité de notre couche fine de NNO aux contraintes mécaniques du substrat. Une simulation utilisant la théorie de Ginsburg-Landau nous permet de reproduire qualitativement la transition métal-isolant en reproduisant correctement la dichotomie entre le refroidissement et leréchauffement. Le chapitre se conclut par une analyse et une simulation de la réponse non-locale de l'échantillon. Cette dernière partie nécessite préalablement une compréhension de la réponse locale afin de pouvoir distinguer la contribution locale du signal de la contribution non-locale.

Le chapitre cinq étudie la transition métal-isolant en la provoquant par

l'effet Joule. Grâce à la lithographie par faisceau d'électrons, des contacts électriques ont été conçus sur des couches minces de NNO, permettant ainsi d'induire la transition électroniquement. En appliquant une tension à nos couches minces de NNO, nous étudions la percolation de filaments métalliques entre les deux électrodes. Le but de ce chapitre est d'étudier la longueur caractéristique de ces filaments en fonction du courant appliqué, de la température et de la qualité de la couche fine. La technique SNOM révèle que bien que le comportement des filaments soit principalement dicté par des paramètres contrôlables (intensité du courant et température), l'effet de la contrainte due au subtrat ne peut être négligé. La réponse non-locale est aussi analysée, avec cette fois une paroi de domaine métal-isolant droite contrôlée par le passage du courant.

Le chapitre six résume les résultats et présente des perspectives pour de futurs projets.

Summary

The insulator-to-metal transition (IMT) in the rare-earth nickelate $NdNiO_3$ (NNO) is a phenomenon of significant interest in condensed matter physics due to its intricate interplay between electronic, structural, and magnetic properties. $NdNiO_3$ belongs to the class of perovskite oxides, which exhibit complex phase transitions that can be tuned by external parameters such as temperature, pressure, and doping. When subjected to changes in temperature or external stimuli, it undergoes a sharp transition to a metallic state, making it an ideal system to explore the mechanisms behind the IMT. Our study will investigate the temperature dependence of the transition in NNO thin films, under a constant epitaxial strain coming from the substrate: lanthanum aluminate ($LaAlO_3$ or LAO).

The measurement technique mainly used for this research is the scattering-type Scanning Near-field Optical Microscopy (s-SNOM). s-SNOM is an advanced technique that combines the spatial resolution of atomic force microscopy (AFM) with the optical sensitivity of an optical microscopy. This powerful method enables the study of material properties at the nanoscale, revealing optical and electromagnetic behaviors that are inaccessible to traditional far-field microscopy due to diffraction limits.

s-SNOM operates by scanning a sharp AFM tip across the surface of a sample while simultaneously measuring the scattered light from the tip's interaction with the sample's local optical properties. This results in the ability to map nanoscopic features of both topography and optical responses, such as surface plasmon polaritons, phonon modes, and material contrasts.

The key advantage of s-SNOM is its ability to achieve sub-wavelength spatial resolution, typically down to 10 nm, while probing the local electromagnetic response in the infrared and visible regions. This makes s-SNOM particularly valuable for investigating nanoscale materials, nanostructures, and phenomena such as local dielectric properties, quantum effects and in our case, inhomogeneous phase transitions. With its combination of high spatial and spectral resolution, s-SNOM has emerged as an indispensable tool in fields ranging from nanophotonics to materials science, providing critical insights into both fundamental and applied research in nanotechnology and condensed matter physics.

The first chapter introduces the nickelate family, of which NNO is a member. Members of this family are distinguished by the different atomic radii of their rare earth elements, which affect the material's crystalline and electronic structure. The effect of rare earth substitution demonstrates the strong link between structural and electronic properties and indicates the ability to control one of these properties through the other. In our case,

this control is achieved through the epitaxial deformation induced by the substrate, LAO, on the thin NNO layer.

The second chapter is a brief presentation of the Ginzburg-Landau model. We will use this model to describe the metal-insulator transition, which is the focus of this research.

The third chapter details the primary measurement technique employed in this study: the SNOM. This method offers numerous advantages, including spatial resolution beyond the diffraction limit, enabling the investigation of both local and non-local responses of the sample. However, to effectively differentiate between these local and non-local responses, this experimental approach must be supported by robust theoretical models and appropriate simulations. These models, such as the point dipole model—which approximates the tip-sample interaction as a dipole induced by the incident field, provide critical frameworks for interpreting SNOM images. By simulating the complex interplay of electromagnetic fields at the nanoscale, these approaches enhance our understanding of the contrast mechanisms and material properties revealed in the microscopy data.

Chapter four begins with the characterization of the thin film using X-ray, conductivity, and reflectivity measurements. The chapter continues with s-SNOM measurements during the metal-insulator transition, revealing a dichotomy between the transition during cooling and heating. This chapter highlights the sensitivity of the metallicity of our NNO thin film to the mechanical stresses of the substrate. A simulation using Ginsburg-Landau theory allows us to qualitatively reproduce the metal-insulator transition by correctly reproducing the dichotomy between cooling and heating. The chapter concludes with an analysis and simulation of the non-local response of the sample. This last part requires a prior understanding of the local response in order to be able to distinguish the local contribution of the signal from the non-local contribution.

Chapter five studies the metal-insulator transition by inducing it through the Joule effect. Through e-beam lithography, electrical contacts have been designed on NNO thin films allowing to induce the transition electronically. By appliying a voltage to our NNO thin films, we study the percolation of metal filaments between the two electrodes. The aim of this chapter is to study the characteristic length of these filaments as a function of the applied current, temperature, and the quality of the thin film. The SNOM technique reveals that although the behavior of the filaments is primarily dictated by controllable parameters (current intensity and temperature), the effect of substrate stress cannot be neglected. The non-local response is also analyzed, this time with a straight metal-insulator domain wall controlled by the flow

of current.
Chapter six summarizes the results and presents perspectives for future projects.

Contents

CHAPTER 1

The physics of nickelates

Nickelates ($RNiO_3$, where R is a rare-earth element) are a class of complex oxide materials that have gained significant attention in recent years due to their rich electronic, magnetic, and structural properties and the interplay between them. The intriguing behavior of nickelates, especially in the context of insulator-to-metal transition (IMT), has made them a subject of intense study in condensed matter physics.

One of the most fascinating features of nickelates is their ability to undergo a IMT as a function of temperature, pressure, and doping. This transition is often driven by subtle changes in their crystal structure and the accompanying modifications to their electronic structure. The phase diagram of nickelates reveals a rich variety of electronic phases existing under different conditions of strain, temperature, and chemical doping.

Strain, in particular, has emerged as a crucial factor in tuning the properties of nickelates. Strain can modify the crystal symmetry and affect the bandwidth of the electronic states thereby controlling the IMT. The manipulation of strain-induced effects provides a powerful tool to explore and engineer the electronic properties of nickelates for potential applications in novel electronic devices and quantum technologies.

In this chapter, we will delve into the phase diagram of nickelates, focusing on the conditions under which the IMT occurs, and explore the effects of strain on their electronic and structural properties.

1.1 Phase diagram of nickelates

Nickelates are compounds belonging to the perovskite family. The perovskites have the form of ABO_3 with A and B different cations. The A cation can be an alkaline metal, an alkaline earth metal, or a rare earth and the B cation a transition metal or post-transition metal. The crystal structure consists of octahedrons formed by oxygen atoms, with the B cation located at its center. The octahedrons are arranged in a cube composed of the A atoms (see Figure 1.1(a)).

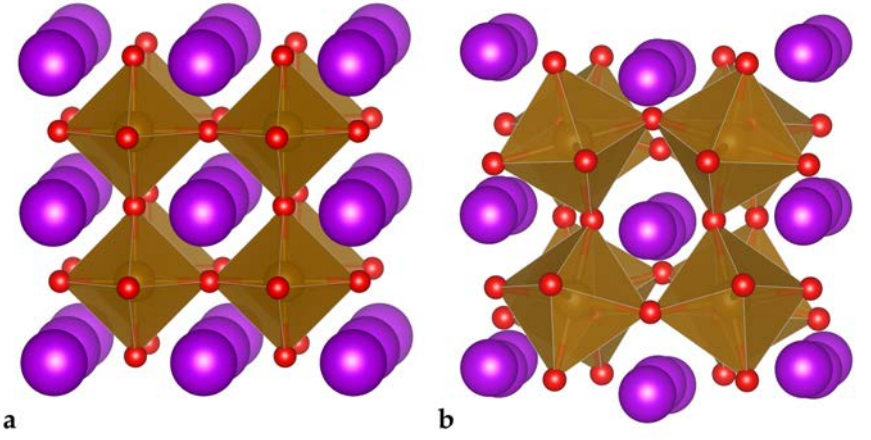

Figure 1.1: Examples of perovskite structures. The A site cations are displayed in purple, oxygen atoms in red, and the B site cations located in the center of the oxygen octahedra in gray. a Cubic perovskite structure of $SrVO_3$. b Orthorhombic structure of $GdFeO_3$. The rotations of the oxygen octahedra, and the displacements of the Gd ions to best accommodate the space in between the oxygen octahedra can be seen. Figure and caption from [1].

In this work, we will focus on the nickelates, a subfamily of perovskite where the B cation is nickel. A key parameter in nickelates is the Goldschmidt tolerance factor, denoted as t:

$$t = \frac{r_{\mathrm{RE}} + r_O}{\sqrt{2}(r_{\mathrm{Ni}} + r_O)} \tag{1.1}$$

with r_{RE}, r_{Ni}, and r_{O} being the ionic radii of the rare earth, the nickel, and the oxygen atoms, respectively. For $t = 1$, the crystal structure is cubic and the angle Ni-O-Ni is 180 degrees. For smaller rare earths, $t < 1$ and the angle Ni-O-Ni is less than 180 degrees. The structure is no longer cubic in this case (see Figure from 1.1(b)). The tolerance factor leads to the phase diagram presented in the Figure 1.2.

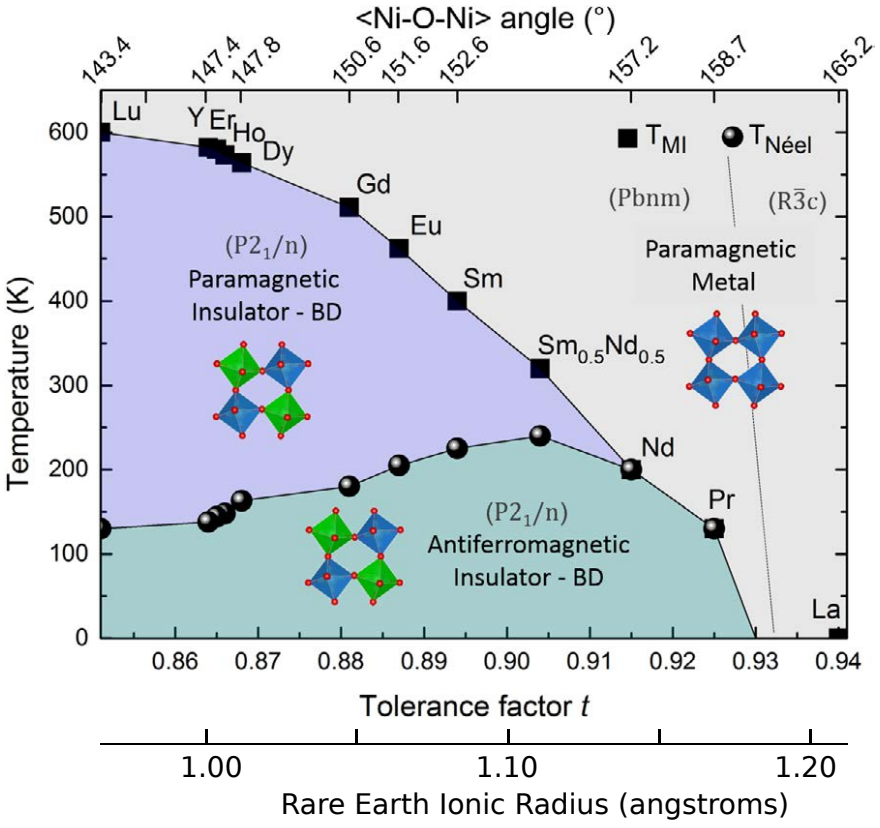

Figure 1.2: Phase diagram of the RNiO$_3$ family summarizing the evolution of the structure as well as the insulator-to-metal and Néel transition temperatures as a function of the tolerance factor t (bottom x axis) and the ⟨Ni–O–Ni⟩ angle Θ (top x axis). BD indicates the bond-disproportionated state. $R\bar{3}c$, $Pbnm$ and $P2_1/n$ indicate space groups corresponding to rhombohedral, orthorhombic and monoclinic crystal structures, respectively. A sketch of the high and low temperature structure is overlaid on the figure. Notice that the scale of the ⟨Ni–O–Ni⟩ angle is non-linear. The t values are calculated from experimental measurements of the R-O and Ni–O distances and therefore differ from the theoretical ones, which assume a purely ionic bonding. Figure and caption adapted from Ref. [2]. The bottom axis (radius) comes from [3].

From the Figure 1.2 and the Equation 1.1, we can see that a small cation radius leads to a lower tolerance factor and higher tilt of the oxygen octahedra. All nickelates but $LaNiO_3$ go through an IMT when cooled down. This transition is concomitant with a structural phase transition which involves a bond disproportionation and an increase in the oxygen octahedra tilt angle. The bond disproportionation, also named breathing distortion, has the structure of a three-dimensional checkerboard of alternating small and big oxygen octahedra (NiO_6). At the same time, a charge ordering

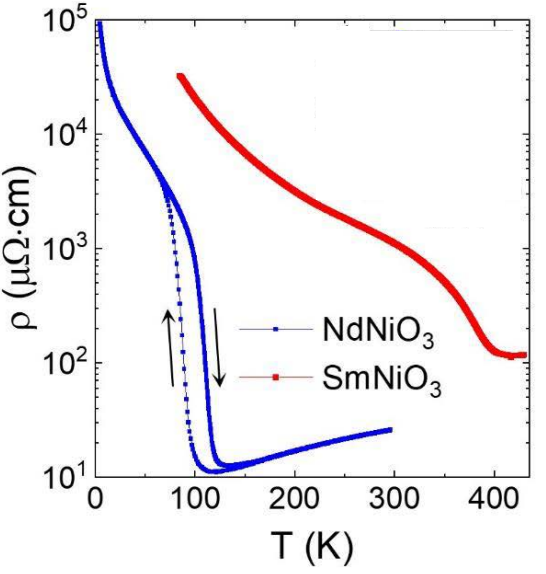

Figure 1.3: (a) Resistivity vs temperature for ≈ 40 nm thick $NdNiO_3$ (blue) and $SmNiO_3$ (red) thin films. The first compound shows a hysteretic behavior marking a first order phase transition. No hysteresis is observed in second compound. Figure and caption adapted from Ref. [4].

occurs resulting in different charge on the nickel atoms at the center of small and big oxygen octahedra. The link between the structural and IMT is discussed in the following section.

As the system cools down, the structure switches from a Pdnm to a $P2_1/n$ symmetry through a first-order transition [5, 6]. The transition from paramagnetic to antiferromagnetic is of the second order [7] for compounds with $T_{\text{Néel}} < T_{\text{MI}}$ but becomes of the first order [8] for compounds with $T_{\text{Néel}} = T_{\text{MI}}$, as it can be seen in Figure 1.3. This behavior can be explained by the magnetic phase requiring the insulating phase to develop [2].

1.2 IMT mechanism

In the nickelates, the magnetic, structural and charge degrees if freedom are linked. We will focus on the link between two of them: the breathing distortion and the charge ordering. We have two scenarios to understand the IMT.
The first one is the low-energy picture [9] . To understand the transition, we need to look at the d orbital of the nickel. Because of the crystal field, the

d orbitals are split three low energy state t_{2g} and two higher energy state e_g(see Figure 1.4).

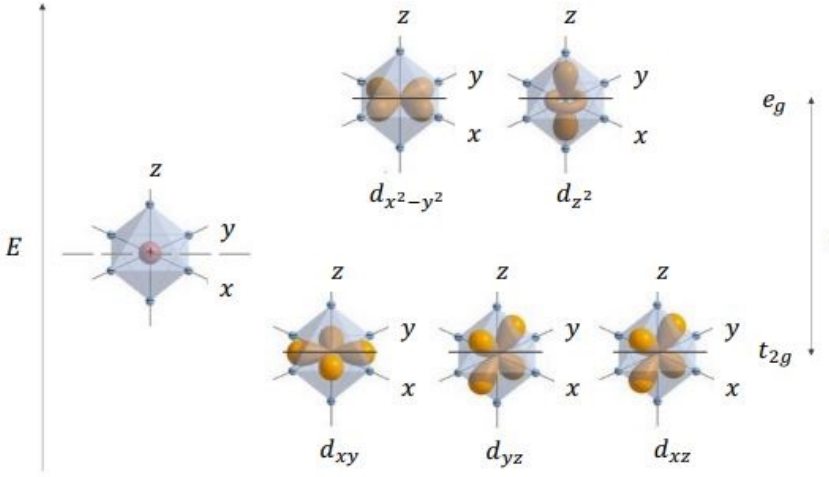

Figure 1.4: Crystal field splitting of the 3d orbitals adapted from Ref. [10].

In this scenario, the breathing mode is accompanied by the following charge disproportionation: $d_i^7 + d_j^7 \longrightarrow d_i^6 + d_j^8$ with i and j being neighboring sites. In this state, the system is insulating as moving an electron from site i to site j would cost Δ_{CF}.

A more recent scenario is the ligand hole picture [11]. In this scenario, the metallic state is d^8L instead of d^7. The system is called a negative charge transfer and self dope by transferring one electron (marked L for ligand) from the oxygen to the nickel atom. Once the bond disproportionation takes place, the electronic state of neighboring atoms switches as follows: $d_i^8 L + d_j^8 L \longrightarrow d_i^8 + d_j^8 L^2$, with the site posessing two ligand holes being the smallest and having zero spin.

The Figure 1.5 presents a simple explanation for the IMT mechanism. In the metallic state, the oxygen octahedra are straight leading to a wider O_{2p} band. The large band width leads to a small (or even negative) gap between the O_{2p} and the Ni_{3d} band, as seen in the bottom of Figure 1.5.
In the insulating state, the octahedra are more tilted leading to a narrower band and the apparition of a gap between the O_{2p} and the Ni_{3d} band, as seen in the top of Figure 1.5.

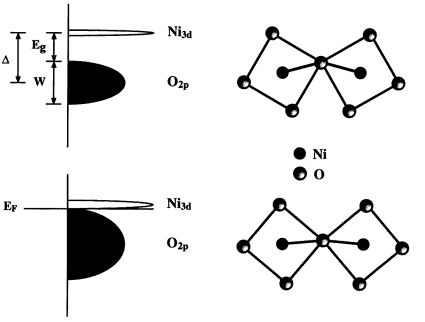

Figure 1.5: IMT in the charge transfer scheme. The top part of the Figure corresponds to an insulating state and the bottom one corresponds to a metallic one. Figure from Ref. [12].

1.3 Strain effect on the phase diagram of nickelates

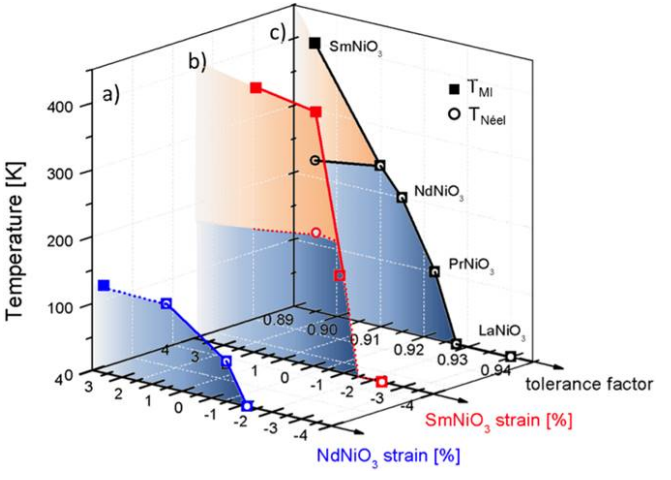

Figure 1.6: Phase diagram of nickelates summarizing the evolution of T_{MI} and $T_{\mathrm{Néel}}$ of strained (a) NNO and (b) $SmNiO_3$ films, compared to the bulk compounds (c).The data the bulk come from [3] and [13]. Figure from Ref. [14].

Strain in a sample can be achieved by applying pressure or by epitaxial strain. Epitaxial strain is obtained by growing a thin film on top of a substrate. The mismatch in lattice parameters between them gives rise to strain in the thin film, either tensile or compressive. Small mismatches create a progressive strain relaxation as strong mismatches (4%) create abrupt

relaxation in the form of dislocation [15]. The Figure 1.6 compares the effect of epitaxial strain and tolerance factor. Compressive strain (negative in Figure 1.6) leads to straightening of the octahedra which is similar to the straightening introduced by the increase of the rare earth radius. The opposite is also true for tensile (positive) strain compared to small rare earth radius. A similar trend is observed in [16] with hydrostatic pressure reducing the T_{MI}.
One must remember that even zero epitaxial strain will still create an additional elastic cost during the structural transition, lowering the T_{MI}. We can therefore not directly compare bulk under pressure and strained thin film.

We selected the $NdNiO_3$ compound as the focus of our study on the IMT due to its pronounced first-order transition. Additionally, $NdNiO_3$ can be epitaxially grown on $LaAlO_3$ (LAO) substrates, which exhibit a small lattice mismatch (-0.5% [17]) with $NdNiO_3$. This minimal mismatch ensures high-quality films without the formation of dislocations or vacancies.

CHAPTER 2

Ginzburg-Landau theory (GLT)

This chapter provides an overview of key concepts in the study of phase transitions, the GLT theory, the nature of first- and second-order transitions, and the associated critical phenomena. The GLT theory offers a phenomenological description of phase transitions where the order parameter continuously changes as the system approaches the critical temperature. In this framework, critical phenomena are characterized by diverging correlation lengths and fluctuations in the order parameter. The distinction between first- and second-order phase transitions is fundamental: first-order transitions are characterized by discontinuous changes in the first derivative of the free energy (such as entropy or volume), whereas second-order transitions exhibit a continuous first derivative, with discontinuities or divergences appearing in the second derivative (such as heat capacity).

A central concept in this theory is the stiffness, which quantifies the resistance of the system to spatial variations of order parameter, playing a critical role in the phase stability. The correlation length, which diverges at the critical point in second-order transitions, reflects the range of these fluctuations and is a key indicator of criticality. To understand the dynamics of such systems, the Langevin Equation is introduced as a tool for modeling the time evolution of the order parameter. Through this chapter, we aim to develop a deeper understanding of these concepts and their relevance to the IMT taking place in the nickelates.

2.1 Symmetry of the order parameter

GLT, using the symmetry arguments and a set of measurable quantities, can describe a system near a phase transition. GLT assumes spatial averaging and local fluctuations and is better suited for systems with long-range interactions. Because GLT is based on symmetry change, GLT cannot describe transitions such as liquid to gaseous transition, where no symmetry change happens. In the case of a transition with symmetry change, the transition has to break the symmetry of the high temperature phase to create a lower symmetry phase. This symmetry breaking is accompanied by an order parameter, that is zero in the high energy phase and changes to a finite value in the low symmetry phase. In the case of nickelates, the breathing distortion is a candidate for the order parameter of the insulating phase. Because the transition is simultaneously structural and electrical, we cannot define the leading parameter in the transition.
Since, during the transition, the order parameter has to go from zero to a finite value, we can expand the free energy of the system in a power series of the order parameter. This expansion should be done with the symmetry of the order parameter in mind. In our case, if we assume that the order parameter is the breathing distortion and the symmetry breaking is the doubling of the unit cell. Neighboring sites are no longer identical with one site having bigger oxygen octahedra than the other (see Figure 2.1).

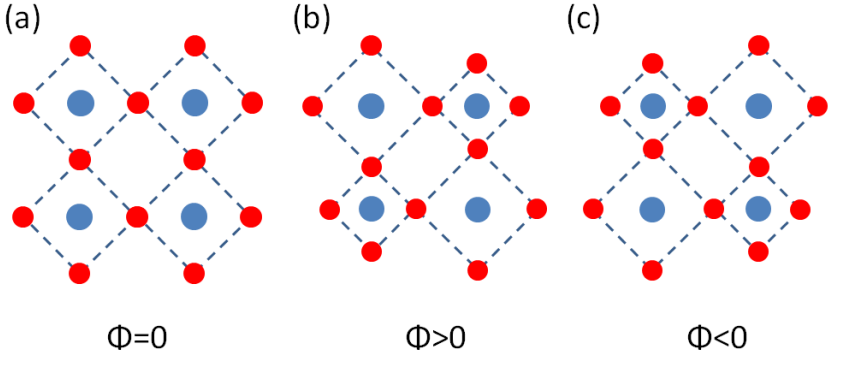

Figure 2.1: Symmetry of the possible order parameter in the nickelates. In (a), the system is in the metallic state with no symmetry broken. (b) and (c) are two states with the same free energy in the insulating state. The oxygen atoms are in red and the nickel in blue.

This freedom of which site has the bigger oxygen octahedra can be translated into free energy being an even function of the order parameter. This can been seen in Figure 2.1 with the (b) and (c) configuration having

the same energy but opposite sign of the free energy. In its simplest form, the free energy can be expend in a Taylor series of even power of the order parameter:

$$f(\Phi, T, T^*) = a\Phi^2 + b\Phi^4 + c\Phi^6 \tag{2.1}$$

with the last term "c" has to be positive to avoid having a minimum of the free energy of the form $\Phi = \pm\infty$. Taking the first derivative of the free energy shows that $\Phi = 0$ is always an extremum of the function.

$$\frac{\partial f(\Phi, T, T^*)}{\partial \Phi} = 2a\Phi + 4b\Phi^3 + 6c\Phi^5 => \frac{\partial f(0, T, T^*)}{\partial \Phi} = 0 \tag{2.2}$$

A second derivative also reveals that this extremum is a minimum if $a>0$ and a maximum if $a<0$.

$$\frac{\partial^2 f(\Phi^2, T, T^*)}{\partial \Phi} = 2a + 12b\Phi^2 + 30c\Phi^4 => \frac{\partial^2 f(0, T, T^*)}{\partial \Phi^2} = 2a \tag{2.3}$$

Therefore, we can express a as $a = a_0(T - T^*)$, where $a_0 > 0$ This substitution ensures that Φ_{min} behaves as desired: it is zero above the transition temperature T^* and finite below, thus minimizing the free energy. The transition temperature T^* can vary across the surface of the sample. Regarding the term "b", its sign determines the different behaviors of the transition.

2.2 Second-order transition

In the case of $b > 0$, we can omit the sixth power of Φ as the fourth one is enough to prevent the free energy from going to an infinite negative value. In this case, we have:

$$f(\Phi, T, T^*) = a_0(T - T^*)\Phi^2 + b\Phi^4 \tag{2.4}$$

This function has minima at either $\Phi = 0$ for $T > T^*$ and $\Phi = \pm\sqrt{\frac{-a_0(T-T^*)}{2b}}$ for $T < T^*$ (Figure 2.2(a)). The phase transition is smooth as the minimum of the free energy continuously shifts from 0 to its finite value (Figure 2.2(b)).

2.3 First-order transition

In this case, b is negative and the sixth power of Φ has to be taken into account. The free energy has the form:

$$f(\Phi, T, T^*) = a_0(T - T^*)\Phi^2 + b\Phi^4 + c\Phi^6 \tag{2.5}$$

with the following minima:

$$\Phi_{\text{min}} = 0 \text{ for } T > T^* \tag{2.6}$$

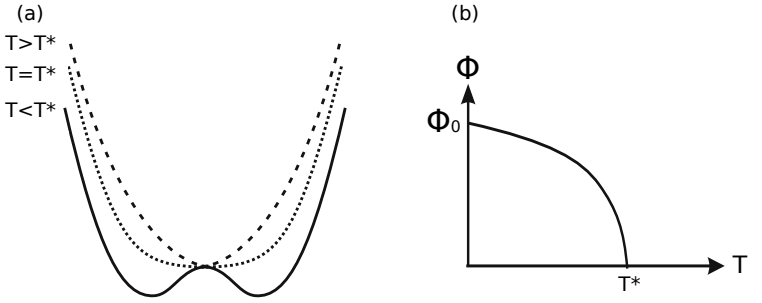

Figure 2.2: (a) Free energy in a second-order transition at different temperature. In this case, the evolution of the minima of the free energy is smooth with no maxima in the free energy blocking the evolution from $\Phi = 0$ to a finite value during the cooling . (b) the continuous evolution of the minima of the free energy as a function of temperature. Adapted from [18].

$$\text{and } \Phi_{\min^*} = \pm\sqrt{\frac{-b + \sqrt{b^2 - 3a_0(T - T^*)c}}{3c}} \text{ for } T < T^{**} = T^* + \frac{b^2}{3a_0c}. \tag{2.7}$$

This transition is behaving quite differently from the second-order one. In this case, in an intermediate temperature $T^* < T < T^{**}$, we have the coexistence of the local minimum at $\Phi = 0$ and two symmetric non-zero minima (see Figure 2.3(a)). The coexistence of those minima creates a hysteretic behavior in this temperature range (Figure 2.3(b)).
Another important key temperature can be identified:

$$T_c = T^* + \frac{b^2}{4a_0c}. \tag{2.8}$$

The free energy is the same for all the minima at this temperature. Above it, the minimum at $\Phi = 0$ has a lower energy than the non-zero ones and below this temperature, the situation is reversed.

2.4 Stiffness and correlation length

Until now, we did not take into account any spatial variation of the order parameter. To do so, we need to add an energy cost to it and the corresponding stiffness parameter: ζ. Without it, each part of the system would lower its energy independently.

$$F(\Phi, T) = \int \left\{ f(\Phi, T, T^*) + \frac{\zeta^2}{2}(\nabla\Phi(\mathbf{r}))^2 \right\} d^d\mathbf{r}. \tag{2.9}$$

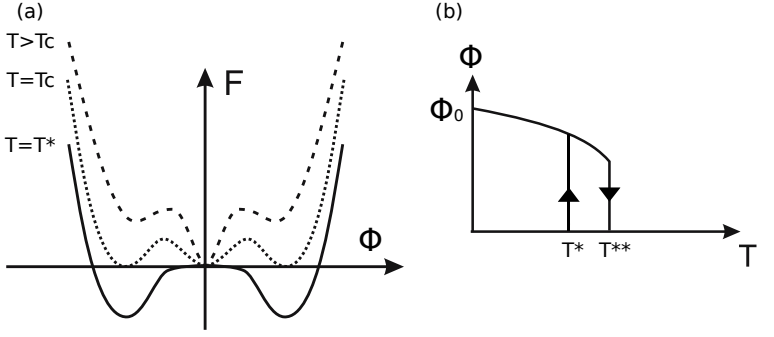

Figure 2.3: (a) Free energy in a first-order transition above the critical temperature T_c, at the critical temperature and at the transition temperature T^*. At the critical temperature, the presence of maxima between local minima creates a memory effect during the transition as the system, if the transition is done slowly, will stay in its local minima even if it is not the lowest minima of the free energy. (b) hysteretic behavior of the order parameter in the first-order phase transition. Adapted from [18].

At the lowest order, the free energy is:

$$F(\Phi,T)=\int\left\{(\Phi-\Phi_{\mathrm{m}})^2\cdot\frac{1}{2}\frac{\partial^2 f}{\partial\Phi^2}\bigg|_{\Phi_{\mathrm{m}}}+f(\Phi_{\mathrm{m}})+\frac{\zeta^2}{2}(\nabla\Phi(\mathbf{r}))^2\right\}d^d\mathbf{r} \tag{2.10}$$

with the second term is the energy cost of spatial variation of the order parameter, Φ_{m} the order parameter at a minimum of the free energy and d the dimension of the system (usually d=3). We can Fourier transform this free energy by taking into account that the order parameter is real:

$$F(\Phi,T)=\int\frac{1}{(2\pi)^d}\left(\frac{1}{2}\frac{\partial^2 f}{\partial\Phi^2}\bigg|_{\Phi_{\mathrm{m}}}+\frac{\zeta^2}{2}k^2)\right)|\Phi(\mathbf{k})|^2 d^d\mathbf{k}. \tag{2.11}$$

By the equipartition theorem, we have:

$$\left\{\frac{1}{2}\frac{\partial^2 f}{\partial\Phi^2}\bigg|_{\Phi_{\mathrm{m}}}+\frac{\zeta^2}{2}k^2)\right\}|\Phi(\mathbf{k})|^2=k_BT \tag{2.12}$$

where k_B is the Boltzmann constant.
We can define the two-site correlation function:

$$g(\mathbf{r})=\langle\Phi(\mathbf{r})\Phi(\mathbf{0})\rangle-\langle\Phi(\mathbf{0})\rangle^2 \tag{2.13}$$

with $g(\mathbf{r})$ the fluctuations of the order parameter. We can Fourier transform $g(\mathbf{r})$ above the transition (where $\langle\Phi(\mathbf{0})\rangle=0$) and assuming that the different

wavevector modes are uncorrelated, we obtain:

$$g(\mathbf{q}) = \langle |\Phi(\mathbf{q})|^2 \rangle \tag{2.14}$$

which can be combined with Equation 2.4 to obtain:

$$g(\mathbf{q}) = \frac{k_B T}{\frac{1}{2}\frac{\partial^2 f}{\partial \Phi^2}\Big|_{\Phi_\mathrm{m}} + \frac{\zeta^2}{2}k^2} \tag{2.15}$$

We can come back to real space by taking the inverse Fourier transform:

$$g(\mathbf{r}) \sim \frac{2k_B T}{\zeta^2}\frac{e^{\frac{-r}{\xi}}}{r^{d-2}}, \text{ for } T \neq T^* \tag{2.16}$$

and

$$g(\mathbf{r}) \sim \frac{2k_B T}{\zeta^2}\frac{1}{r^{d-2}}, \text{ for } T = T^* \tag{2.17}$$

with

$$\xi = \frac{\zeta}{\sqrt{\frac{\partial^2 f}{\partial \Phi^2}\Big|_{\Phi_\mathrm{m}}}} \tag{2.18}$$

with ξ the correlation length which diverges at $T = T^*$ and $T = T^{**}$. This correlation length is the ratio between the stiffness ζ, which favors big correlation lengths, and the term $\sqrt{\frac{\partial^2 f}{\partial \Phi^2}\Big|_{\Phi_\mathrm{m}}}$ which favors small correlation lengths to minimize locally the free energy.

2.5 Temporal evolution of the order parameter: Langevin equation

Until now, we focused only on the evolution of the free energy with respect of temperature. To describe the temporal evolution of the order parameter $\Phi(x, y, t)$, we use the Langevin Equation [19]:

$$\frac{\partial \Phi}{\partial t} = -\lambda \frac{\partial F}{\partial \Phi} + \nu g \tag{2.19}$$

with λ the system diffusion constant, ν the noise intensity and $g(x, y, t)$ the Gaussian noise centered to zero and with zero self-correlation. These two variables are not independent and are linked by the fluctuation-dissipation theorem. For simulations, we need a spatial distribution of the transition temperature, $T^*(x, y)$ and an initial distribution of the order parameter, $\Phi(x, y, 0)$. By then discretizing the Equation of the free energy and the Equation of Langevin, we can simulate the evolution of our system.

CHAPTER 3

Principles of the near-field (NF) optical spectroscopy

This chapter introduces the fundamental concepts necessary to understand the signals detected in Scattering-type Scanning Near-field Optical Microscopy (s-SNOM) measurements. After an introduction on the NF, we focus on the key quantity giving contrast between the metallic and insulating phase: the dielectric function. Using the Drude-Lorentz model as a framework, we explain how the dielectric function is linked to measurements via Fresnel's coefficients and provide an introduction to surface polaritons.

3.1 The evanescent nature of the NF

When students are first introduced to electromagnetic waves, they typically are taught to disregard solutions decaying exponentially with distance, as the electric field would not reach a detector. To overcome this limitation and access such fields (the NF), techniques like aperture scanning near-field optical microscopy and scattering scanning near-field optical microscopy (s-SNOM) were developed. The NF provides an opportunity to overcome the diffraction limit of light, as its exponential decay in one direction is compensated by an increase in momentum in another direction. For a fixed momentum of norm k, we can express the relation as: $\mathrm{k} = \sqrt{\mathrm{k_x^2} + \mathrm{k_y^2} + \mathrm{k_z^2}}$. By fixing $\mathrm{k_z}$ imaginary, we obtain a field decaying exponentially in the z direction ($e^{i\mathrm{k_z}} = e^{-|\mathrm{k_z}|}$) while the momentum in the xy-plane becomes larger than the norm k. To detect such a field, any measurement technique must

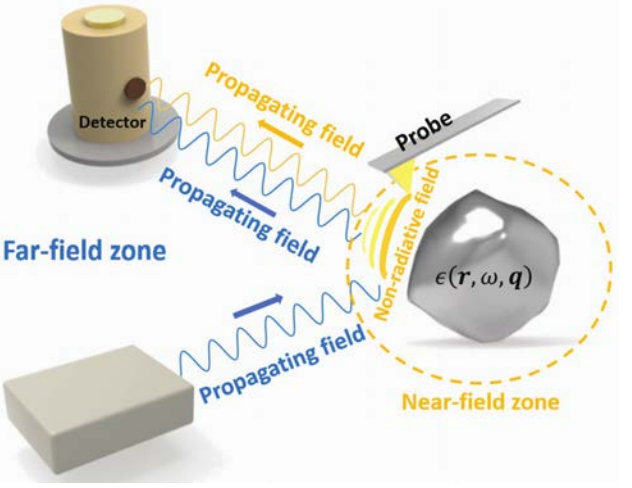

Figure 3.1: Far-field (blue) and NF (yellow) measurements, accessing the propagating field and the evanescent field, respectively. Figure and caption from Ref. [20].

account for the decaying nature of the field.

The s-SNOM technique detects NF by placing a probe close to the studied object and collecting the scattered light (Figure 3.1). The probe, a metalized atomic force microscopy (AFM) tip, is illuminated by a laser and serves as both a NF emitter and receptor, converting evanescent waves into propagating ones and vice versa. Similarly, as the AFM tracks changes in a mechanical harmonic oscillator coupled to the sample studied, the s-SNOM records change in an electrical harmonic oscillator (a polarized dipole in the AFM tip) coupled to the same sample. One key quantity probed during s-SNOM measurement is the dielectric function of the sample directly below the AFM tip. For this reason, this chapter will start by presenting a model for this physical quantity.

3.2 The Drude-Lorentz model

To calculate the sample's response to an electric field and subsequently model the s-SNOM signal, we must first model the dielectric function of the sample. For this purpose, we will use an extension of the Drude theory, which describes the behavior of free electrons within a metal. It is based on the following assumptions:

-The electrons behave as a non-interacting gas.

-The electrons can collide with the immobile positive ions of the metal. When they do, they reset their speed and become in equilibrium with the

local temperature.

Using those assumptions [21], we can obtain the optical conductivity:

$$\sigma(\omega) = \frac{\sigma_0}{1 - i\omega\tau} \text{ with } \sigma_0 = \sigma(0) = \frac{ne^2\tau}{m_e} \tag{3.1}$$

with n the electron density, m_e the electron mass, τ the time between two consecutive collisions. The optical conductivity σ is linking the current density J and the electric field as following:

$$J(\omega) = \sigma(\omega)E(\omega) \tag{3.2}$$

We can link this quantity to the dielectric function with [22]:

$$\epsilon(\omega) = \epsilon_\infty + \frac{i\sigma(\omega)}{\epsilon_0\omega} \tag{3.3}$$

with ϵ_0 the vacuum permittivity and ϵ_∞ corresponding to the high-frequency dielectric constant. This value is a simplification of Lorentzian oscillators well above the frequency range investigated. The optical conductivity can be rewritten in a more useful way as:

$$\sigma(\omega) = \frac{\epsilon_0\omega_p^2\tau}{1 - i\omega\tau} \text{ with } \omega_p^2 = \frac{ne^2}{\epsilon_0 m_e} \tag{3.4}$$

with ω_p known as the plasma frequency. For frequency lower than ω_p, the electromagnetic field is reflected and for frequency above ω_p, the electromagnetic field can penetrate the metal. This effect can be seen in gold, where the plasma frequency is in the visible range, giving gold its color. The Drude model was created for metals but can be extended. In the Drude model, there is one Lorentzian centered at zero with a scattering rate of $\frac{1}{\tau}$. This Lorentzian is known as the Drude peak and represents the response of the free electrons in the metal. The Drude-Lorentz model removes the condition for the Lorentzian to be centered at zero and considers a sum of Lorentzian:

$$\epsilon(\omega) = \epsilon_\infty + \sum_j \frac{\omega_{pj}^2}{\omega_{0j}^2 - \omega^2 - i\frac{1}{\tau_j}\omega} \tag{3.5}$$

with ω_{0j}, ω_{pj} and $\frac{1}{\tau_j}$ the position, the spectral weight and the width of the j-th Lorentz oscillator respectively.

Each Lorentzian represents oscillations of bond charges such as phonons. Putting ω_{0j} to zero recovers the Drude term.

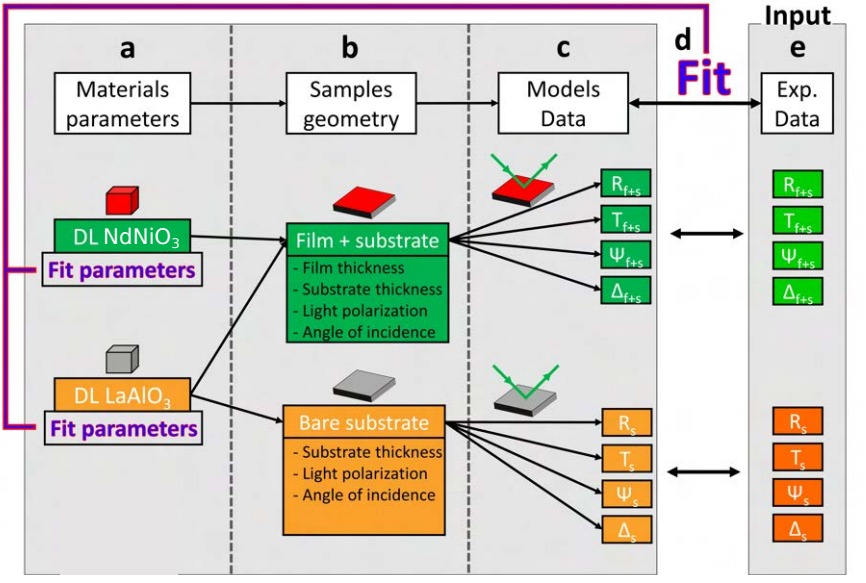

Figure 3.2: Figure and caption adapted from Ref. [23]. Schematic representation of the fitting process. (a) Drude-Lorentz models of the film material ($NdNiO_3$) and the substrate material ($LaAlO_3$). After the fit, the parameters provide an optical conductivities based on the models. (b)) Specification of samples and experimental parameters such as the thickness of the film. (c) Optical quantities such as reflectance (R) and transmittance (T) deduced from Drude-Lorentz models, samples and experimental parameters using Fresnel equations. (d) Fit of the models parameters from experimental data and optical quantities coming from the models. The fit is an iterative loop. (e)) Experimental data.

3.3 Drude-Lorentz fitting using "Reffit" sofware

An effective way to obtain the dielectric constant of a material is to fit data with the Drude-Lorentz model. Data coming from classical optical measurements such as reflectivity, transmission or ellipsometry can be fitted using the program Reffit. The Figure 3.2 summarize the steps of a fitting procedure. Using an initial guess for the dielectric constant (Figure 3.2(a)) as well as the configuration of the experiment, such as the sample thickness (Figure 3.2(b)), the angle of incidence of the light and its polarization (Figure 3.2(c)), Reffit can compare the calculated model with the experimental data (Figure 3.2(d)). Reffit will find the best fitting parameters to match the measurement using the Levenberg-Marquardt algorithm in an iterative loop. One strength of Reffit is its ability to fit multiple different sets of measurements at the same time with a common dielectric function. This feature is present in Figure 3.2 where the reflectivity of a bare substrate and a thin film on the substrate are simultaneously fitted using the same Drude-Lorentz model parameters for the substrate material.

3.4 Fresnel's reflection coefficient

The Fresnel's reflection coefficient, r_p and r_s, represents the ratio of the reflected light to the incident light, polarized perpendicularly and parallel respectively to a reflective plane. The r_p coefficient is a crucial parameter for calculating the s-SNOM signal, as the technique relies on the light reflected from the sample to the AFM tip. In order to calculate the r_p of a sample we need both the dielectric function of the sample and its geometry. For the reflection at an interface between two materials [24] with normal angle of incidence, we have:

$$r_\mathrm{p} = \lim_{q_i \to 0} \frac{q_1\epsilon_2 - q_2\epsilon_1}{q_1\epsilon_2 + q_2\epsilon_1} = \frac{\epsilon_2 - \epsilon_1}{\epsilon_2 + \epsilon_1} \tag{3.6}$$

with ϵ_n the dielectric function of the n^{th} material, $q_\mathrm{n} = \sqrt{\epsilon_\mathrm{n} q_0^2 - q^2}$ the out of plan momentum in the n^{th} material and $q_0 = \frac{w}{c}$ the momentum in free space.

For our measurement, we will have a thin film of NNO on top of bulk LAO substrate. In this case, from top to bottom, we will have the indices 0 for the vacuum above the sample, 1 for the NNO thin film and 2 for the LAO bulk. In this case, internal reflections can occur inside the thin film, leading to the formula:

$$r_\mathrm{p} = r_{0\to1} + \frac{t_{0\to1} t_{1\to0} r_{1\to2} e^{i2k_1 d}}{1 - r_{1\to0} r_{1\to2} e^{i2k_1 d}} \tag{3.7}$$

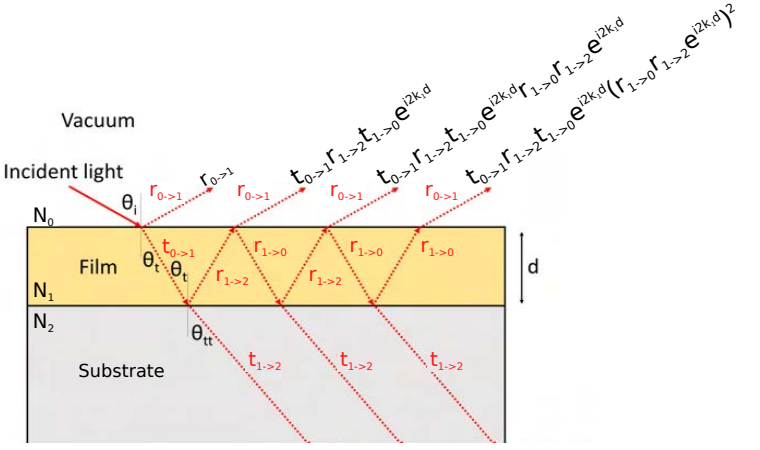

Figure 3.3: Reflection coefficient of a film composed of an infinite number of internal reflection. The incident light is perpendicular to the film in our case; however, for clarity, the angle θ is shown as non-zero in this figure. Figure adapted from Ref. [23].

with $r_{n\to m} = \frac{q_n\epsilon_m - q_m\epsilon_n}{q_n\epsilon_m + q_m\epsilon_n}$, $t_{n\to m} = \frac{2q_n\epsilon_m}{q_n\epsilon_m - q_m\epsilon_n}$ the Fresnel coefficient for reflection and transmission respectively and d the thickness of the film.

Equation 3.7 can be recovered from the Figure 3.3. The first term $r_{0\to1}$ corresponds to the reflection on the top of the thin film. The second term corresponds to the sum of internal reflection inside the thin film of the form: $t_{0\to1}r_{1\to2}t_{1\to0}e^{i2k_1d}\left(r_{1\to0}r_{1\to2}e^{i2k_1d}\right)^n$ with n the number of internal reflection going from 0 to infinity. Each term has to enter the film, be reflected by the bottom of the film and leave the film which lead to the factor $t_{0\to1}r_{1\to2}t_{1\to0}e^{i2k_1d}$ with a phase picked up from going through the film twice. The term $r_{1\to0}r_{1\to2}e^{i2k_1d}$ comes from the reflection from the top of the film, bottom of the film and again the phase picked up from going through the film twice. This last back and forth can happen an infinite number of times and as the total outgoing light is the sum of all possible paths, Equation 3.7 is written as a geometric series.

3.5 Surface polaritons (SP) and edge polaritons (ED)

A polariton is the result of the coupling between an electromagnetic wave and a polarization excitation within a material. When the excitation is confined to a surface and exhibits an exponential decay as it moves away from the surface, it is referred to as a SP.

As the electric field of a SP decays exponentially with the surface distance, they are detected by the s-SNOM technique. Using Maxwell's equations, the

following conditions are needed to support SPs [25]:

$$\epsilon_1 \cdot \epsilon_2 < 0 \text{ and } \epsilon_1 + \epsilon_2 < 0 \tag{3.8}$$

with $\epsilon_{1,2}$ the dielectric function of the top and bottom medium respectively. We also get the dispersion of the SP:

$$k_x = k \left(\frac{\epsilon_1 \epsilon_2}{\epsilon_1 + \epsilon_2} \right)^{1/2} \tag{3.9}$$

with k_x the in-plane momentum of the SP and k the momentum of light in free space. As we can see, at the interface of vacuum ($\epsilon_1 = 1$) and metal ($\epsilon_2 < 0$), the momentum of the SP is bigger than the free space momentum. It means that to excite SP using light, we need an additional momentum provided by a sharp scatterer close to the surface. The scatterer can be the AFM tip or a sharp edge of the sample or gold reference/electrode.

The hybridization between light and polarization that occurs at a two-dimensional interface, resulting in SPs, can also happen at a one-dimensional interface. In this one-dimensional case, the resulting polariton is referred to as an edge polariton (EP), which exhibits a shorter wavelength (approximately 80% of the wavelength of a SP [26, 27]).

In the case of a more complex configuration than a bulk sample surface, a common practice is to plot $\mathrm{Im}(r_\mathrm{p})$ as a function of both the light frequency and momentum. Any pole in the r_p corresponds to a bound mode localized at the surface [28, 29]. This plot allows us to predict the s-SNOM signal by reading the plot at the frequency of the light used and momentum close to the inverse of the radius of the AFM tip of the experiment. A high value of r_p leads to high polarisability of the tip-sample system and leads to a higher s-SNOM signal (see section 4.3). Plotting the quantity $\mathrm{Im}(r_\mathrm{p})$ also has the advantage of revealing any SPs as their dissipation will lead to a branch of high $\mathrm{Im}(r_\mathrm{p})$.

This technique was applied in reference [30], where the authors observed the hybridization of graphene's surface plasmon with the surface phonons of the underlying SiO_2 substrate. The hybridization process is depicted in Figure 3.4(b-d), where two surface phonons—one weak at 850 cm^{-1} and the other strong at 1128 cm^{-1} initially appear as flat (b) modes before hybridizing with the graphene plasmon.

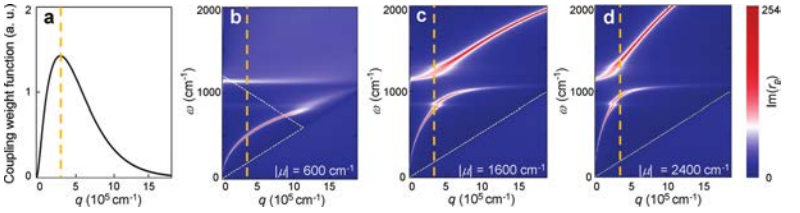

Figure 3.4: (a) The NF coupling weight function which peak at the inverse of the size of the AFM tip. This function will be introduced later in section 4.3. (b-d) imaginary part of the reflection coefficient $im(r_{\mathrm{p}}(q, w))$ of graphene at different chemical potentials on top of SiO_2. Figure from Ref. [30].

CHAPTER 4

s-SNOM as a nanoscale optical probe

Scattering-type Scanning Near-field Optical Microscopy (s-SNOM) is a hybrid technique that combines the capabilities of optical spectroscopy and atomic force microscopy (AFM). This powerful tool integrates the spectral sensitivity of a spectrometer with the high spatial resolution of AFM , the latter being necessary to resolve the phase coexistence present in our NNO thin film during the IMT. After an overview of the AFM technique, the subsequent sections will describe how the near-field signal is extracted and the types of information it provides. This chapter concludes by a presentation of the setup used.

4.1 Atomic force microscopy basic concept

We will now explain how a metallic probe is maintained close to the sample surface. To do so, we will refer to chapters 1 to 3 of Ref. [31].

The AFM technique can extract local mechanical properties (such as Young's modulus) of the sample surface. In the most basic mode of operation, the quantity extracted is the sample's topography. An AFM operates by scanning closely a target surface with its probe, a sharp tip ($\approx$ 50 nm), while monitoring the interactions between the tip and the surface. The relative movement between the tip and the sample surface is controlled by piezoelectric motors. These motors rely on piezoelectric materials, which deform under an applied electric potential and generate an electric potential when deformed. With precision in the nanometer range, these motors are

essential for the fine control of the tip relative to the sample surface. However, piezoelectric motors exhibit deviations from ideal linear behavior, such as creep and hysteresis (see Figure 4.1(a)). To correct these behaviors, two methods are commonly used: open-loop and closed-loop control.

The open-loop method involves measuring the non-linearity of the piezoelectric motors and using this calibration to adjust all subsequent scans. This technique is advantageous in terms of compactness, as the correction occurs as a post-process. In our case, open-loop control is used since the AFM is housed within a cryostat, and calibration measurements have been performed to account for non-linear temperature effects. However, regular re-calibrations are necessary, as the non-linearity of the piezoelectric motors may change over time.

The closed-loop method, on the other hand, employs an external sensor to continuously correct the motor movement in real time. While this approach is less compact than the open-loop method, it requires no recalibration, offering a more consistent solution over time. The open-loop method is used in our case as our s-SNOM is embedded in a cryostat and compactness is critical.

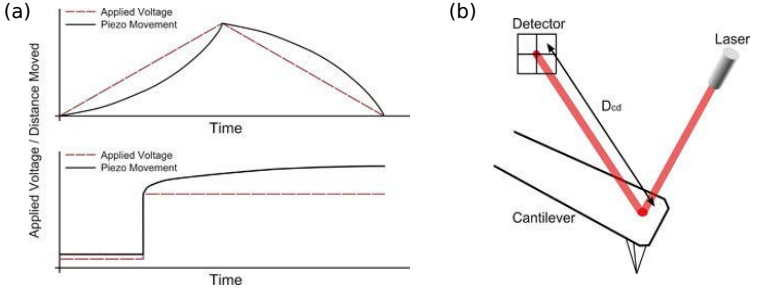

Figure 4.1: a) Examples of non-linear behavior in piezoelectric scanners. Top: hysteresis; when a voltage ramp is applied to the piezo, the response is non-linear. Bottom: creep; after an impulse is applied to the piezo, the movement continues in the same direction. b) Schematic diagram of the optical lever sensor. In an optical lever, as the end of the cantilever bends the position of the laser spot on the detector changes. As the cantilever–detector distance D_{cd} is large, a small movement of the cantilever causes a large change in the laser spot position at the detector. Figure adapted from Ref. [31].

The force sensor, which measures the interaction between the tip and the sample surface, is an optical lever. The optical lever operates as follows: Any force acting on the tip causes the cantilever to bend. This deflection is continuously monitored by focusing a laser on the back of the cantilever, with the reflected beam directed onto a photodetector. The photodetector measures the position of the laser spot, which corresponds to the cantilever's deflection. The large distance between the cantilever and the detector en-

hances the sensitivity of the system (see Figure 4.1(b)). The force-distance curve (Figure 4.2) is used to convert the measured laser deflection into the tip-sample distance. Instead of the static deflection of the laser, a measure of the dynamic oscillation of the cantilever is possible.

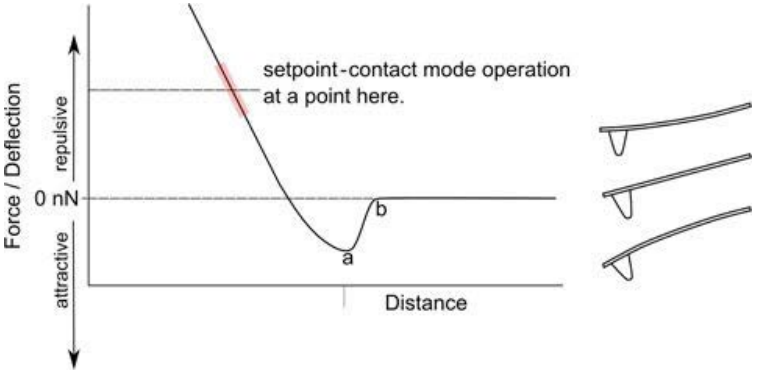

Figure 4.2: Simplified force-distance curve showing contact (repulsive region) scanning regime. A deflection–distance curve, which is the raw data from which a force-distance curve is measured, has a similar shape. Right: illustration of probe bending in each regime. Figure from Ref. [31].

Different regimes can be identified in Figure 4.2 : non-interacting at a high distance, attractive at medium distance and repulsive at close distance. Different measurement modes exist exploiting different parts of the force-distance curve. Contact mode would stay on the repulsive part, non-contact mode is on the attractive part and tapping or intermittent contact mode would be on both. For the s-SNOM technique, tapping mode is used as the near-field interaction studied is (very) close range and varies exponentially with the tip-sample distance.

Tapping mode is a widely used imaging mode in AFM, where the cantilever oscillates near its resonant frequency and intermittently contacts the surface during the scan. Unlike contact mode, where the tip maintains constant contact with the sample surface, tapping mode minimizes continuous contact, reducing the risk of sample damage and allowing for high-resolution imaging of delicate or soft surfaces.

In tapping mode, the cantilever is driven to oscillate with an external signal, typically at or near its natural resonance frequency, using a piezoelectric actuator. As the AFM tip scans the surface, it taps the surface at regular intervals and passes through possible contamination layer (water for example). The interaction between the tip and the surface causes changes in

the amplitude, phase, or frequency of the oscillation.

The changes in the oscillation parameters are used to generate topographical images of the surface. By measuring the phase shift or amplitude reduction during the interaction between the tip and the surface, tapping mode provides both height and mechanical property information (such as stiffness or adhesion) of the sample. The technique is particularly advantageous for imaging soft materials, biological samples, and nanoscale features, offering superior resolution with minimal lateral force.

4.2 Background Suppression in s-SNOM

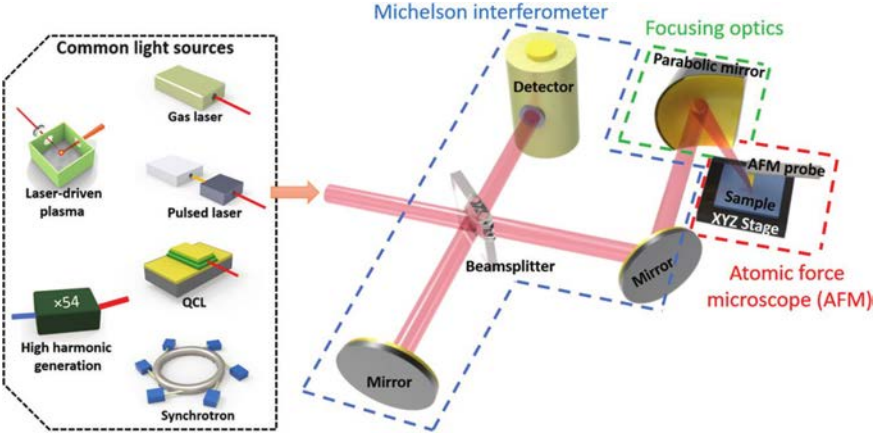

Figure 4.3: A typical s-SNOM setup with from left to right: a light source, a detection scheme (here a Michelson interferometer and a detector), focusing optics and an AFM. Figure from Ref. [20].

Now that we introduced the AFM part of the s-SNOM, we can turn our attention to the optical part of it. The detection scheme (middle of Figure 4.3) has the important task of filtering the NF signal from background ones such as scattering from the cantilever, from the sample or the shaft of the tip. Multiple techniques exist to filter this background signal. The following presentation of different detection schemes is adapted from Ref. [20].

Almost all techniques use the fact that the NF interaction between the tip and the sample is highly non-linear on the tip-sample distance as opposed to a linear or constant background signal. Demodulation of the signal using high harmonics of the AFM tip's frequency allows us to select this NF signal.

As our AFM tip resonance frequency is around 270 kHz, the second and the third harmonic are used as the fourth harmonic is in the range of MHz and falls beyond the bandwidth of the detection electronics. We use the

pseudo-heterodyne detection scheme for measurement but "downgrade" to self-homodyne and homodyne for calibration.

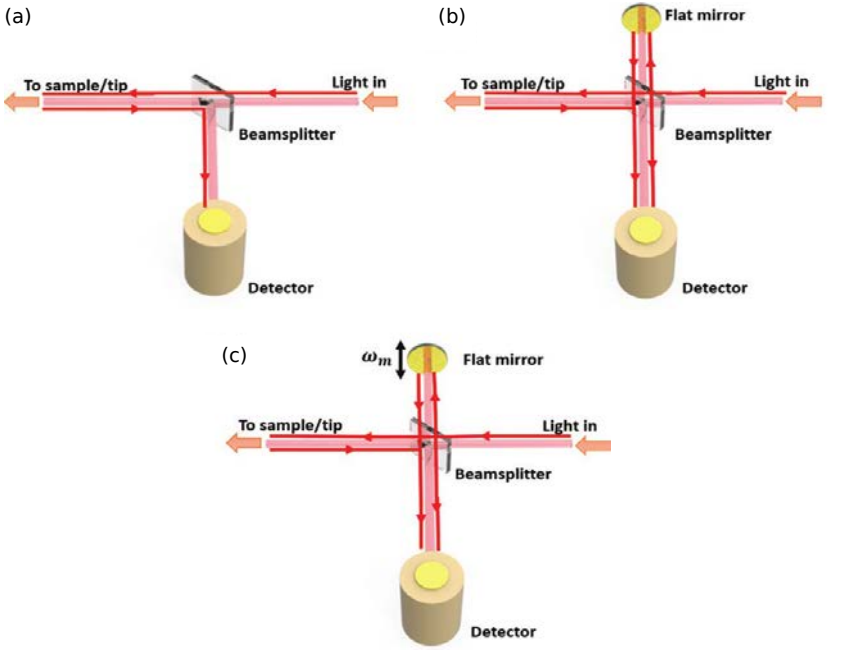

Figure 4.4: SNOM detection schemes . (a) Self-homodyne. (b) Homodyne. (c) Pseudo-heterodyne. We use the pseudo-heterodyne for measurement and self-homodyne and homodyne for calibration. Adapted from [20].

4.2.1 The self-homodyne detection

As indicated in Figure 4.4(a), this detection scheme is the simplest of the three. The detector is only sensitive to the intensity of the electric field:

$$I = (E_{\mathrm{N}} + E_{\mathrm{B}})(E_{\mathrm{N}}^{*} + E_{\mathrm{B}}^{*}) \tag{4.1}$$

with E_{N} and E_{B} being the near field and background electric field respectively. The * indicates the complex conjugate. The intensity can be written as:

$$I = |E_{\mathrm{B}}|^2 + 2|E_{\mathrm{B}}||E_{\mathrm{N}}|\cos(\phi_{\mathrm{B}} - \phi_{\mathrm{N}}) + |E_{\mathrm{N}}|^2 \tag{4.2}$$

with ϕ_{B} and ϕ_{N} the background and NF phase respectively. In most cases, the background signal has the highest intensity and the first term is dominating,

followed by the second term. The third term is too weak to be detected. After demodulation with the tip frequency, only the second and third terms remain. This detection scheme is only sensitive to the amplitude of the NF as the background phase (ϕ_B) is a free parameter. During calibration, a time consuming step is the alignment of the parabolic mirror that focuses light into the AFM tip. To facilitate the alignment, we block the light passing to the mirror of our Michelson interferometer in order to have a signal of the form $|E_B||E_N|\cos(\phi_B - \phi_N)$. This signal contains the NF information but with a lower spatial resolution as the background signal is affected by the diffraction limit. This lower resolution ease the first step of the alignment of the parabolic mirror. AFM tip have often (once a week) to be replaced because of their coating degradation each time requiring a realignment of the parabolic mirror.

4.2.2 The homodyne detection

The homodyne detection scheme is a self-homodyne detection with an added reference arm. Phase can be detected through the interference inside the Michelson interferometer. The new signal has the following form:

$$I = (E_N + E_B + E_R)(E_N^* + E_B^* + E_R^*) \tag{4.3}$$

with E_R the added reference electric field. We can develop the formula:

$$I = |E_B|^2 + |E_R|^2 + 2|E_B||E_R|\cos(\phi_B - \phi_R) + 2|E_R||E_N|\cos(\phi_R - \phi_N) \tag{4.4}$$

$$+2|E_B||E_N|\cos(\phi_B - \phi_N) + |E_N|^2. \tag{4.5}$$

The first three terms can be removed with demodulation of the tip tapping frequency. We are left with:

$$I = 2|E_R||E_N|\cos(\phi_R - \phi_N) + 2|E_B||E_N|\cos(\phi_B - \phi_N) + |E_N|^2. \tag{4.6}$$

The first term is expected to be the more intense followed by the second. The second term cannot be ignored in a reflective sample and the background signal will be present in the final signal. By changing the position of the mirror (beam path length), we have control over the reference phase and can recover the NF phase. Consecutive scans must be done with a quarter-wavelength change in the optical path to get both NF amplitude and phase. We use this detection scheme during calibration to align the orientation of the reference mirror.

4.2.3 The pseudo-heterodyne detection

The pseudo-heterodyne detection scheme is similar to the heterodyne detection but it uses a vibrating mirror in the reference arm of the Michelson

interferometer. By demodulating the signal at the sum or difference of a high harmonic of the tip tapping frequency and the frequency of vibration of the reference mirror, we can select the cross term of the reference electric field and the near field signal the same way it is done in the heterodyne detection scheme (Figure 4.5). Since we add the frequency of the oscillation of the reference mirror, we will express fields coming from the sample as Fourier series of the frequency of the tip, Ω, and the field coming from the reference path as the frequency of the oscillating mirror, M.

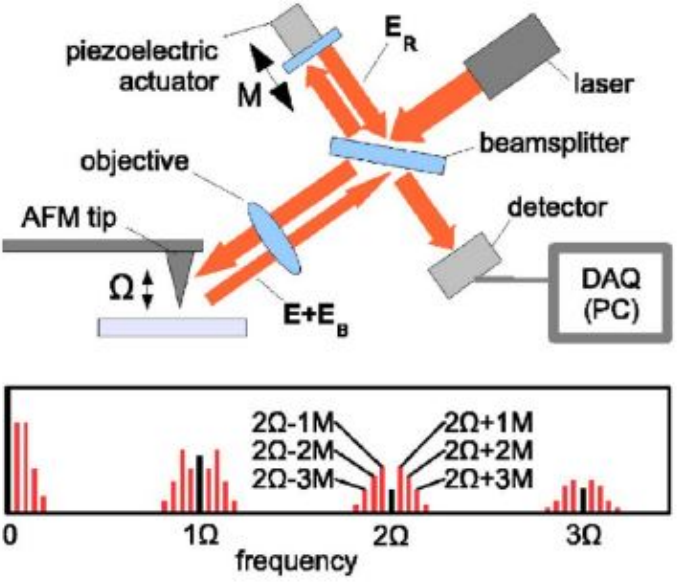

Figure 4.5: Pseudohetorodyne detection scheme. E, E_{R} and E_{B} are the near-field electric field, the reference signal and the background signal respectively. Adapted from [32].

The following derivation comes from Ref. [32]. From the sample, we get the following fields:

$$E_{\mathrm{N}} = E_0 \sum_n e^{in\Omega t}\sigma_{\mathrm{N},n} \text{ and } E_{\mathrm{B}} = E_0 \sum_n e^{in\Omega t}\sigma_{\mathrm{B},n} \tag{4.7}$$

We can sum them up to E_{S}, the scattered field.

$$E_{\mathrm{S}} = \sum_n e^{in\Omega t}\tau_n \tag{4.8}$$

with $\tau_n = \sigma_{\mathrm{N},n} + \sigma_{\mathrm{B},n}$. From the reference path, we have the field:

$$E_{\mathrm{R}} = \rho e^{i\gamma \sin(Mt) + i\Phi_{\mathrm{R}}} \text{ with } \gamma = \frac{2\pi\Delta x}{\lambda} \tag{4.9}$$

with M the modulation frequency ,γ the modulation depth, Λ the wavelength and Δx the amplitude peak to peak of the oscillation of the mirror. This field can be written in a Fourier series of the frequency M:

$$E_{\mathrm{R}} = \sum_m \rho_m e^{iMmt} \text{ with } \rho_m = \rho J_m(\gamma) e^{i\Phi_{\mathrm{R}} + im\frac{\pi}{2}} \tag{4.10}$$

with J_m the Bessel function of the first kind at the mth order. By choosing the frequency M lower than Ω, we obtain intensity spectra of the form shown in Figure 4.5 with a cross term of $E_{\mathrm{B}}E_{\mathrm{N}}$ present at harmonics of Ω and the targeted cross term $E_{\mathrm{R}}E_{\mathrm{N}}$ at sideband of the harmonics with $f_{n,m\neq 0}$. By rewriting τ_n as $s_n e^{i\Phi_n}$ and selecting signal at a sideband, we have:

$$u_{m,n\neq 0} = 2\rho J_m(\gamma) s_n \cos(i\Phi_{\mathrm{R}} + im\frac{\pi}{2} - \Phi_n). \tag{4.11}$$

We can see that successive sidebands alternate between being proportional to the real (cos) and imaginary (sin) part of the Fourier coefficient τ_n. We can recover τ_n by combining two signal amplitudes:

$$\tau_n = k\left[\frac{u_{n,j}}{J_j(\gamma)} + i\frac{u_{n,l}}{J_l(\gamma)}\right] \tag{4.12}$$

with $k = \frac{e^{i\Phi_{\mathrm{R}}}}{2\rho}$, j an even and l an odd integer. By choosing $l = 1$, $j = 2$ and $\gamma = 2.63$, we can equalize $J_j(\gamma)$ and $J_l(\gamma)$ which gives:

$$\tau_n = 2.16k(u_{n,2} + iu_{n,1}). \tag{4.13}$$

The modulation depth of $\gamma = 2.63$ is found by adding a slow oscillation in the path length of the reference beam. By changing the modulation depth while monitoring the first and second sideband, we can select the value of γ that leaves the first sideband (real part) constant with the second sideband (imaginary part) that slowly oscillates. The slow oscillation is only used for calibration and is removed during the measurements.

We further simplify the signal by removing the prefactor by normalizing the measurement with a reference. By choosing high harmonic n, we have $\tau_n \simeq \sigma_n$ since the near field has a faster spatial decay than the background field. We will later refer the the modulus and the argument of τ_n as the near field amplitude and near field phase respectively.

4.3 SNOM signal modeling

This section presents a minimalist model designed to identify the physical quantities probed by s-SNOM measurements. To facilitate analytical cal-

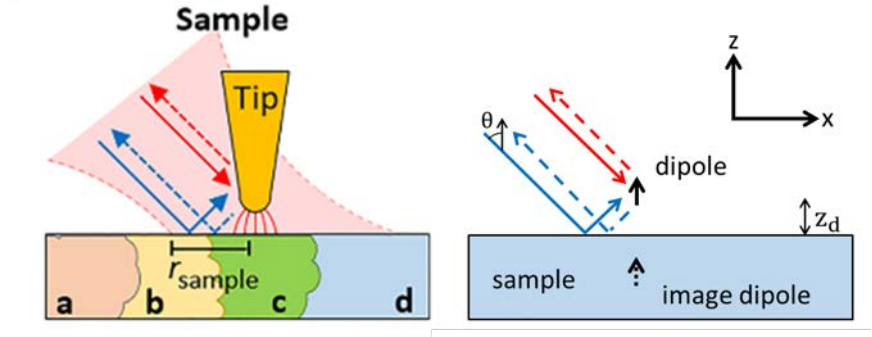

Figure 4.6: Illustration of of a s-SNOM experiment in the realistic case (a) and simplified one (b) with red arrows and blue arrows the direct and indirect illumination respectively. (a) A metalized AFM tip above an inhomogeneous sample is illuminated by an external source (red area) . Adapted from reference [33]. (b) simplified situation were the afm tip is replaced by a point dipole.

culations, this model will require several approximations (see Figure 4.6). The following development is adapted from [34]. This section will have the following steps: First, we will approximate the AFM tip with a point dipole. Secondly, we will describe the external field surrounding the dipole. Then, we will interest ourselves in the field emitted by the dipole and the effect of the back reflection of the sample. This step will be in momentum space as the reflective index of the sample depends on the momentum of the field. Lastly, we will speak about the spatial tapping of the dipole and its effect on the signal.

The first approximation done is regarding the probe of our experiment: the metalized AFM tip. Because of its elongated shape, we can approximate the tip as a directional dipole along the z-direction, z being perpendicular to the plane of the sample surface.

$$\mathbf{d} = \hat{\alpha} \cdot \mathbf{E} = \alpha \cdot \begin{pmatrix} 0 & 0 & 0 \\ 0 & 0 & 0 \\ 0 & 0 & 1 \end{pmatrix} \cdot \mathbf{E} = \alpha \cdot \mathbf{E_z} \tag{4.14}$$

with $\mathbf{d}$ the dipole vector and $\hat{\alpha}$ the polarizability tensor. This dipole is near a sample surface and exposed to a far-field illumination. Both the direct and reflected fields affect the dipole. All fields will have the temporal dependence of the illuminating field : $e^{-i\omega t}$. The electromagnetic waves in vacuum have the wavelength: $\lambda_0 = \frac{2\pi}{q_0} = \frac{2\pi c}{\omega}$ and momentum: $q_0 = \frac{\omega}{c}$.

If we take an incoming illuminating plane wave with an angle θ, we have the following relation:

$$\mathbf{k}_{\text{inc}} = q_0 \begin{pmatrix} \sin\theta \\ 0 \\ -\cos\theta \end{pmatrix}; \mathbf{k}_{\text{refl}} = q_0 \begin{pmatrix} \sin\theta \\ 0 \\ \cos\theta \end{pmatrix} \tag{4.15}$$

$$\mathbf{E}_{\text{inc}} = E_0 \begin{pmatrix} \cos\theta \\ 0 \\ \sin\theta \end{pmatrix}; \mathbf{E}_{\text{refl}} = E_0 \cdot r_{\text{p}}(q_0 \sin\theta, \omega) \cdot \begin{pmatrix} -\cos\theta \\ 0 \\ \sin\theta \end{pmatrix} \tag{4.16}$$

with $\mathbf{E}_{\text{inc}}$ the incoming electric field and $\mathbf{E}_{\text{refl}}$ the reflected one. We have as the total field above the sample surface :

$$\mathbf{E}_{\text{ext}}(\mathbf{r}) = \mathbf{E}_{\text{inc}} e^{i\mathbf{k}_{\text{inc}}\mathbf{r}} + \mathbf{E}_{\text{refl}} e^{i\mathbf{k}_{\text{refl}}\mathbf{r}} \tag{4.17}$$

$$= E_0 \begin{pmatrix} \cos\theta(e^{iq_0(x\cdot\sin\theta - z\cdot\cos\theta)} - r_{\text{p}}(q_0\sin\theta,\omega)\cdot e^{iq_0(x\cdot\sin\theta + z\cdot\cos\theta)}) \\ 0 \\ \sin\theta(e^{iq_0(x\cdot\sin\theta - z\cdot\cos\theta)} + r_{\text{p}}(q_0\sin\theta,\omega)\cdot e^{iq_0(x\cdot\sin\theta + z\cdot\cos\theta)}) \end{pmatrix}. \tag{4.18}$$

We suppose that the dipole is sensitive only to the z-component of the total field:

$$E_{\text{ext,z}} = E_0 \sin\theta (e^{-iq_0 z\cdot\cos\theta} + r_{\text{p}}(q_0\sin\theta,\omega)\cdot e^{iq_0 z\cdot\cos\theta}). \tag{4.19}$$

For the next step, we need the field created by the dipole in the momentum space. For elastic scattering, we have the following relation linking the momentum of the field of the dipole with the momentum of the illuminating filed:

$$q_0^2 = k_x^2 + k_y^2 + k_{\text{z}}^2 = q^2 + k_{\text{z}}^2 \text{ with } q \text{ the momentum in plane.} \tag{4.20}$$

We can identify the near-field case:

$$q > q_0 \Rightarrow k_{\text{z}} = \sqrt{q_0^2 - q^2} \text{ is imaginary.} \tag{4.21}$$

In the basis of plane waves and with z_d the height of the dipole, the electric field of the dipole is [35]:

$$\mathbf{E}(\mathbf{r}) = \frac{iq_0^2}{2\pi} \int_{-\infty}^{\infty} dk_x \int_{-\infty}^{\infty} dk_y \frac{1}{k_{\text{z}}} \left[\begin{pmatrix} 0 \\ 0 \\ d \end{pmatrix} - \frac{d \cdot k_{\text{z}}}{q_0^2} \cdot \begin{pmatrix} k_x \\ k_y \\ -k_z \end{pmatrix} \right] \cdot e^{iq\cos(\phi)x + iq\sin(\phi)y + ik_{\text{z}}\cdot|z-z_d|} \tag{4.22}$$

$$= \frac{iq_0^2 \cdot d}{2\pi} \int_{-\infty}^{\infty} dk_x \int_{-\infty}^{\infty} dk_y \begin{pmatrix} \frac{-k_x}{q_0^2} \\ \frac{-k_y}{q_0^2} \\ \frac{q^2}{q_0^2 k_{\text{z}}} \end{pmatrix} \cdot e^{iq\cos(\phi)x + iq\sin(\phi)y + ik_{\text{z}}\cdot|z-z_d|} \tag{4.23}$$

$$= \frac{id}{2\pi} \int_{-\infty}^{\infty} dk_x \int_{-\infty}^{\infty} dk_y \begin{pmatrix} -k_x \\ -k_y \\ \frac{q^2}{k_{\text{z}}} \end{pmatrix} \cdot e^{iq\cos(\phi)x + iq\sin(\phi)y + ik_{\text{z}}\cdot|z-z_d|} \tag{4.24}$$

$$= \frac{id}{2\pi} \int_0^{\infty} dq \int_0^{2\pi} d\phi \begin{pmatrix} -q^2\cos(\phi) \\ -q^2\sin(\phi) \\ \frac{q^3}{k_{\text{z}}} \end{pmatrix} \cdot e^{iq\cos(\phi)x + iq\sin(\phi)y + ik_{\text{z}}\cdot|z-z_d|}. \tag{4.25}$$

We are only interested in the field the z direction:

$$E_{\text{z}}(\text{z}) = \frac{id}{2\pi} \int_0^{\infty} dq \frac{q^3}{k_{\text{z}}} e^{ik_{\text{z}}|z-z_d|} \int_0^{2\pi} d\phi e^{iq\cos(\phi)x + iq\sin(\phi)y}. \tag{4.26}$$

The integral from 0 to 2π is equal to 2π:

$$E_{\mathrm{z}}(\mathrm{z}) = id \int_0^\infty dq \frac{q^3}{k_{\mathrm{z}}} e^{ik_{\mathrm{z}}|z-z_d|} \ . \tag{4.27}$$

We need the field from the image dipole at the position of the dipole to capture the interaction between the AFM tip and the sample:

$$E_{\mathrm{refl,z}}(z_d) = i \cdot d \int_0^\infty dq \cdot r_{\mathrm{p}}(q) \frac{q^3}{k_{\mathrm{z}}} e^{ik_{\mathrm{z}}2z_d} \tag{4.28}$$

with $r_{\mathrm{p}}(q)$ the reflection coefficient of the sample at momentum q. The calculation of the coefficient $r_{\mathrm{p}}(q)$ is presented in section 3.4.
The dipole is affected by the external field and its reflected field off the sample:

$$d = \alpha[E_{\mathrm{ext,z}}(z_d) + di \int_0^\infty dq \cdot r_{\mathrm{p}}(q) \frac{q^3}{k_{\mathrm{z}}} e^{ik_{\mathrm{z}}2z_d}] \tag{4.29}$$

$$\Rightarrow d(z_d) = \frac{\alpha E_{\mathrm{ext,z}}(z_d)}{1 - i\alpha \int_0^\infty dq \cdot r_{\mathrm{p}}(q) \frac{q^3}{k_{\mathrm{z}}} e^{ik_{\mathrm{z}}2z_d}} \tag{4.30}$$

$$d(z_d) = \alpha_{\mathrm{eff}}(Z_d) E_{\mathrm{ext,z}}(Z_d) \text{ with } \alpha_{\mathrm{eff}} = \frac{\alpha}{1 - i\alpha \int_0^\infty dq \cdot r_{\mathrm{p}}(q) \frac{q^3}{k_{\mathrm{z}}} e^{ik_{\mathrm{z}}2z_d}}. \tag{4.31}$$

In the near field approximation $z_d \ll \lambda_0 \Leftrightarrow q_0 z_d \ll 1$:

$$E_{\mathrm{ext,z}} = E_0 \mathrm{sin}\theta(1 + r_{\mathrm{p}}(q_0 \mathrm{sin}\theta, \omega)). \tag{4.32}$$

We do a change of variable, $q = q_0 \cdot q'$ and $k_{\mathrm{z}} = q_0 \cdot k'_{\mathrm{z}}$:

$$\alpha_{\mathrm{eff}} = \frac{\alpha}{1 - i\alpha q_0^3 \int_0^\infty dq' \cdot r_{\mathrm{p}}(q_0 \cdot q') \frac{q'^3}{k'_{\mathrm{z}}} e^{ik'_{\mathrm{z}} q_0 2z_d}} \tag{4.33}$$

$$\alpha_{\mathrm{eff}} = \frac{\alpha}{1 - iq_0^3 \alpha G'} \tag{4.34}$$

with G' in the limit $z_d \ll \lambda_0 <=> q_0 z_d \ll 1$ and $k_{\mathrm{z}}(q) = \sqrt{1 - q^2}$:

$$G' = \int_0^\infty dq' \cdot r_{\mathrm{p}}(q_0 q') \frac{q'^3}{\sqrt{1 - q'^2}} e^{i\sqrt{1-q'^2} 2q_0 z_d} \ . \tag{4.35}$$

In the near-field limit, $q' >> 1$ and $\sqrt{1 - q'^2} = iq'$;

$$G' \approx \int_0^\infty dq' \cdot r_{\mathrm{p}}(q_0 q') \cdot (-iq'^2) \cdot e^{-q' 2q_0 z_d} \ . \tag{4.36}$$

We can put in back in the effective polarizability:

$$\alpha_{\text{eff}} \approx \frac{\alpha}{1 - q_0^3 \alpha \int_0^\infty dq' \cdot r_{\text{p}}(q_0 q') q'^2 e^{-q' 2 q_0 z_d}} \tag{4.37}$$

$$\alpha_{\text{eff}} \approx \frac{\alpha}{1 - \alpha \int_0^\infty dq \cdot r_{\text{p}}(q) q^2 e^{-2 q z_d}} \tag{4.38}$$

$$\alpha_{\text{eff}} \approx \frac{\alpha}{1 - \alpha G} \text{ ; with } G = \int_0^\infty dq \cdot r_{\text{p}}(q) q^2 e^{-2 q z_d} \, . \tag{4.39}$$

The function G controls the tip's polarizability change due to the tip-sample interaction. This function can be split into two parts: the first part, referred to as the coupling weight function [30], is: $q^2 e^{-2 q z_d}$ and can be seen in Figure 4.7. For the maximum tip-sample interaction, we need the lowest z_d. For an AFM tip approximated by a sphere with the dipole in its center, this is achieved when the AFM tip touches the surface of the sample. It means that the minimum distance between the sample and the surface is the tip radius: $z_d = r_{tip}$.

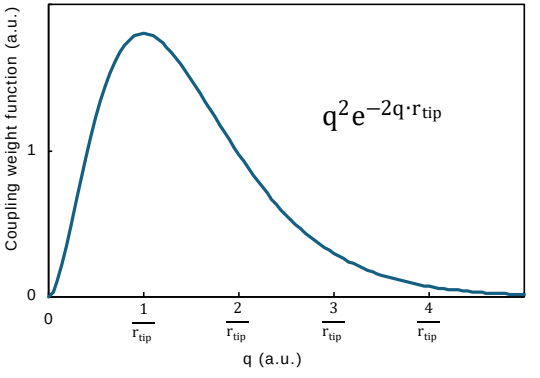

Figure 4.7: The coupling weight function of the AFM tip. The maximum of this function is at momentum equal to the inverse of the AFM tip radius. For a typical tip radius (50 nm), this maximum is around $2 \cdot 10^5$ cm^{-1}.

The second part of the function G is $r_{\text{p}}(q)$. It is the reflectivity of the sample at a finite q value. Because of the coupling weight function, we can say that we mostly probe the reflectivity of the sample at momentum equal to the inverse of the AFM tip radius ($\frac{1}{r_{tip}}$).

If we focus on the detected signal of the s-SNOM, we have that the signal detected is proportional to the illumination intensity, the illumination factor squared (accounting for both the incoming and outgoing paths) and the effective polarizability.

$$S(z_d) \propto E_0 \cdot \sin(\theta)^2 (1 + r_{\text{p}}(q_0 \sin\theta, \omega))^2 \cdot \alpha_{\text{eff}} \tag{4.40}$$

$$S(z_d) \propto E_0 \sin(\theta)^2 (1 + r_\mathrm{p}(q_0 \sin\theta, \omega))^2 \frac{\alpha}{1 - \alpha \int_0^\infty dq \cdot r_\mathrm{p}(q) q^2 e^{-2qz_d}}. \quad (4.41)$$

if $\alpha \int_0^\infty dq \cdot r_\mathrm{p}(q) q^2 e^{-2qz_d} \ll 1$, we can simplify to:

$$S(z_d) \propto E_0 \sin(\theta)^2 (1 + r_\mathrm{p}(q_0 \sin\theta, \omega))^2 \alpha^2 \int_0^\infty dq \cdot r_\mathrm{p}(q) q^2 e^{-2qz_d} \quad (4.42)$$

with the coupling function $r_\mathrm{p}(q) q^2 e^{-2qz_d}$ peaking around $\frac{1}{r_{tip}}$, we can further simplify as:

$$S(z_d) \propto r_\mathrm{p}(\frac{1}{r_{tip}}) \, . \quad (4.43)$$

We have derived a simplified expression for the s-SNOM signal: the Fresnel reflection coefficient r_p, a complex value, evaluated at a momentum near the inverse of the AFM tip's radius.

In reality, the s-SNOM is working in the tapping mode, where the tip oscillates with an peak-to-peak amplitude z_amp and a frequency $\Omega \ll \omega$. The optical signal is detected at higher harmonics $\Omega_n = n\Omega$. The signal $\tilde{s}_n = s_n e^{i\phi_n}$ at a given harmonic n can be obtained by the Fourier transform of $S(z_d)$:

$$\tilde{s}_n = \frac{1}{2\pi} \int_0^{2\pi} e^{in\varphi} S[z_d(\varphi)] d\varphi, \quad (4.44)$$

where $z_d(\varphi) = z_\mathrm{min} + z_\mathrm{amp}(1 - \cos\varphi)$ and $\varphi = \Omega t$ is the oscillation phase.

4.3.1 Fixed dipole approximation

To enable computer simulation, a simplified model is preferred. Instead of exciting the dipole with a plane wave, we fix the dipole strength and eliminate the far-field illumination. This simplification eliminates the need to extract the near-field signal from the far-field background while focusing on the key quantity $r_p(q)$. We have z_d as the dipole height and z_p the probing height:

$$E = E_\mathrm{direct} + E_\mathrm{imag} \, . \quad (4.45)$$

The direct field is constant for a fixed dipole strength and fixed position (see A.2). We are left with the image field as the direct one is a constant value.

$$\frac{E_\mathrm{refl}}{d} \approx \int_0^\infty dq \cdot r_\mathrm{p}(q) q^2 e^{-q(z_d + z_p)} \, . \quad (4.46)$$

Using the Figure 4.7, we have that the coupling function is maximal around momentum of the inverse of the dipole distance:

$$\frac{E_\mathrm{refl}}{d} \propto r_\mathrm{p}(\frac{2}{z_p + z_d}) \, . \quad (4.47)$$

We arrived at a similar expression to Eq.4.43, but with a significantly simpler configuration, involving a fixed dipole strength and no vertical oscillation. This approximation offers a strong potential for qualitatively simulating the s-SNOM signal. This approach has been successfully applied in [27].

4.4 Interferometric detection of surface polaritons (SP)

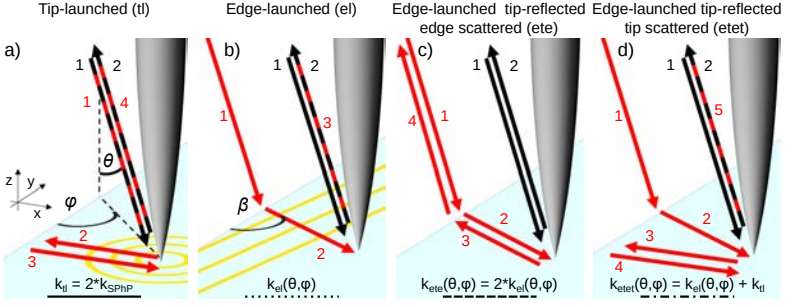

Figure 4.8: Multiple plasmon pathways between an edge and the AFM tip. The black arrows represent scattering and backscattering off the tip. a) Plasmons are radially launched from the tip and reflected by the edge. Hence, the detected interference pattern has twice the spatial frequency of the plasmon and its electric intensity decays geometrically by $d^{-\frac{1}{2}}$ with d the distance between the tip and the edge. b) Plasmons launched by the edge and scattered by the tip with the momentum $k_{(\theta,\phi)}$ depending on the angle of the incoming light. c) Plasmon are launched by the edge, reflected by the tip and scattered by the edge. d) Plasmons are launched by the tip, reflected by the edge and scattered by the tip. Figure from Ref. [36].

The signal detected using the s-SNOM technique is twofold: one component, described in section 4.3, contains information about the reflection coefficient of the sample directly beneath the AFM tip. The second component is associated with SP, which can propagate over micrometer distances. In a simple scenario, the edge of a flake acts both as an emitter and a reflector of SP (see 4.8(a) and (b).

SP manifest as interference patterns on the surface, with any reflection doubling the momentum of the resulting pattern. Since SP decay over distance, the pure local signal can be measured in a homogeneous sample or at a location far from defects and edges, as demonstrated in Figure 4.9.

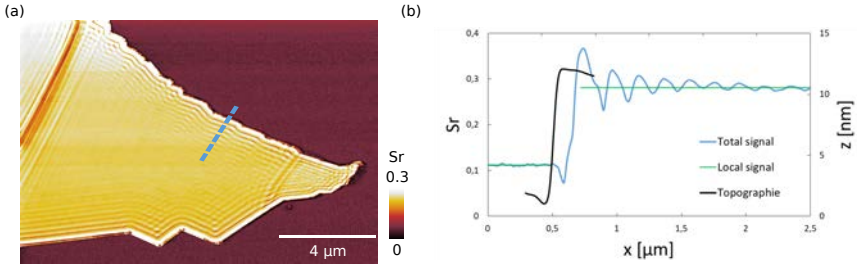

Figure 4.9: Interference pattern of SP on a boron nitride flake. (a) Near field amplitude image of a boron nitride (hBN) flake on silicon oxide (SiO_2) substrate at 1460 cm^{-1}. (b) Line profile taken from (a) at the blue dash line. SiO_2 before 0.5 μm and hBN after 0.5 μm. The black line represents the topography, the blue one represents the amplitude of the detected signal and the green line corresponds to the amplitude of the signal in the absence of SP.

4.5 Finite Element Analysis, COMSOL

Finite Element Analysis (FEA) is a powerful numerical technique used to solve complex physical problems by discretizing a system into smaller, simpler subdomains called finite elements. This method is particularly effective for solving partial differential equations (PDEs), which are commonly encountered in engineering and physics applications. One of the most prominent PDEs in the field of electromagnetics are Maxwell's equations, which govern the behavior of electric and magnetic fields in a variety of scenarios, such as wave propagation, electromagnetic interference, and radiation. These equations, in their time-harmonic form, describe the interaction between electric and magnetic fields, and they are essential for understanding phenomena like electromagnetic wave propagation, diffraction, and the behavior of antennas and waveguides.

COMSOL Multiphysics is a comprehensive simulation software platform that employs FEA to solve Maxwell's equations for electromagnetic fields. In particular, COMSOL's "Electromagnetic Waves" module allows users to model and simulate the behavior of electromagnetic fields in both the frequency and time domains, providing insights into a wide range of applications, including antenna design, waveguide analysis, and electromagnetic compatibility. Solving Maxwell's equations with FEA in COMSOL enables the simulation of complex electromagnetic phenomena in irregular geometries and material environments, where analytical solutions are not readily available.

A key consideration when solving Maxwell's equations using FEA in COMSOL is the accurate resolution of the electromagnetic waves, which requires careful adaptation of the computational spatial mesh to the wavelength of the propagating waves. The mesh represents the discretized model

of the problem domain, and its resolution directly affects the accuracy of the simulation results. To properly capture the wave behavior, the mesh must be sufficiently fine, particularly in regions where the electromagnetic fields undergo significant variation. The general guideline is that the mesh elements should be smaller than or equal to a fraction of the wavelength of the electromagnetic wave being simulated, with typical mesh element sizes being on the order of 1/10th or smaller than the wavelength.

If the mesh is too coarse relative to the wavelength, important features of the electromagnetic fields such as field gradients, wave interference, or resonant modes may not be accurately represented, leading to errors in the simulation results. Conversely, a mesh that is too fine can increase computational cost without yielding a proportionate improvement in accuracy. Therefore, mesh adaptation is crucial for balancing computational efficiency with the need for precision in simulating electromagnetic wave phenomena.

Through the integration of FEA with Maxwell's equations and adaptive meshing techniques, COMSOL provides a versatile platform for simulating electromagnetic phenomena in a wide range of applications. The ability to customize the mesh based on the wavelength ensures that simulations are both accurate and computationally efficient, making COMSOL an indispensable tool for researchers and engineers in the field of electromagnetics.

4.6 Cryogenic s-SNOM

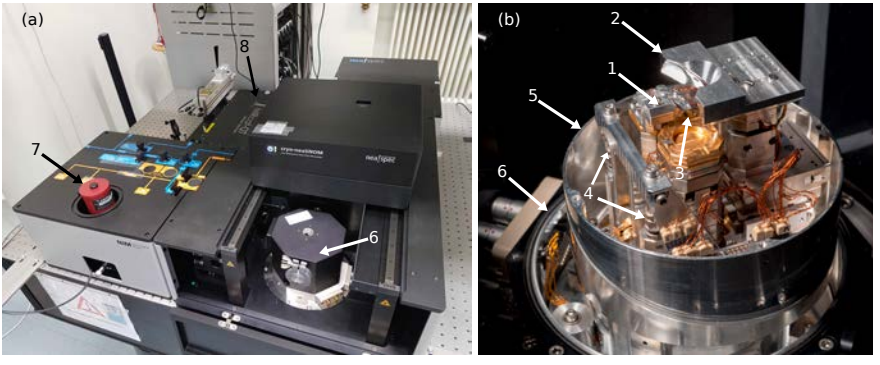

Figure 4.10: pictures of our cryo-SNOM. (a) view of the whole system. (b) view of the cryostat. The numbers highlight the following elements: 1 is the AFM tip holder, 2 is the parabolic mirror, 3 is the sample holder below, 4 are springs that mechanically isolate the AFM system, 5 is the cold shield, 6 is the outside of the cryostat, 7 is the mercury cadmium telluride (MCT) detector and 8 is a quantum cascade laser.

Our s-SNOM is built inside a cryostat to allow temperature control. The

cooling is done with a closed helium cycle with a temperature range of 10 to 350 K. This temperature flexibility of the measurement is done at the cost of some complications of AFM. Because of the cryostat, the AFM is in an open loop, meaning that the AFM motors operate without feedback. This results in a higher sensitivity to the hysteretic behavior of the piezoelectric motors. The vibrations of the pumps and compressor are also additional complications compared to a room temperature system. Our AFM system sits on 3 springs (two springs are visible in Figure 4.10 at number 4) to limit the mechanical noise.

The Figure 4.10 presents briefly our system. The three main elements (1 to 3 in Figure 4.10 respectively) are the AFM tip, the parabolic mirror and the sample holder. These three elements each sit on three piezoelectric motors allowing a XYZ position control of each component. Once we overcome these technical difficulties, we gain access to rich physical behaviors, such as the one presented in this thesis.

CHAPTER 5

Temperature driven IMT

This chapter investigates the IMT in NNO thin films on $LaAlO_3$ (LAO). It begins with a characterization of the sample's thickness and quality through X-ray diffraction. The IMT is initially identified via far-field reflectivity and temperature-dependent resistance measurements. Subsequently, scanning near-field optical microscopy (SNOM) was employed to observe spatial inhomogeneities during the transition. Finally, using Ginzburg-Landau simulations, we explain and reproduce the most prominent patterns observed during the IMT.

5.1 Sample preparation

Using radio-frequency magneto sputtering, the epitaxial NNO thin film (10 nm or 29 unit cell) was grown on oriented (001) LAO. As a reference for the s-SNOM signal, Au stripes of around 40 nm thick were deposited on part of the sample surface. To characterize the sample, X-ray diffraction, transport measurement and infrared reflectivity measurements were taken (see Figure 5.1(a), (b) and (c) respectively).

One can see, from Figure 5.1(b) and (c), that the hysteresis in the IMT takes place between 93 to 120 K with a sharper transition during the cooling as compared to the warming. As discussed in section 2.3, this information allows us to determine T^*, T^{**} and a_0 of the free energy in the Ginzburg-Landau model. This transition is taking place at a much lower temperature

compared to bulk NNO ($\sim$ 200 K for bulk in Figure 1.2). This difference is attributed to the strain induced by the LAO substrate [14]. Because of this strong link between the strain and the transition temperature, the next section focus on the substrate used in this experiment.

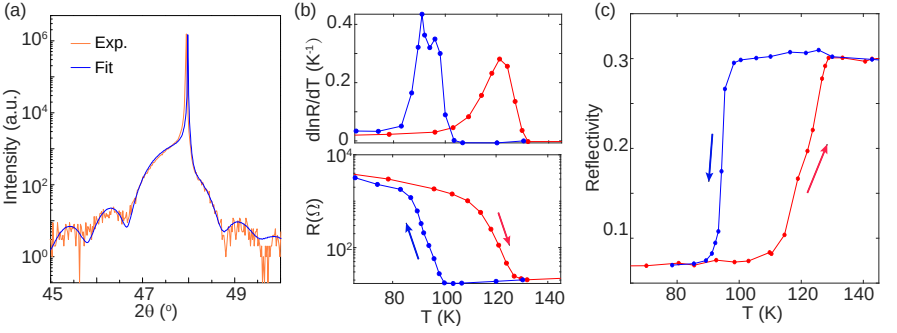

Figure 5.1: Characterization of the NNO(10 nm)/LAO sample. (a) Measured X-ray diffraction curve, which can be fitted well with the NNO thickness of 29 unit cells (around 10 nm). (b,c) Temperature-dependent resistance (b) and far-field optical reflectivity measurements (c) during the cooling (blue) and warming (red) stages. The reflectivity data is for a light frequency of 939 cm^{-1}.

5.2 The $LaAlO_3$ crystal structure

Due to its perovskite structure, $LaAlO_3$ is widely used as a substrate for various perovskite oxide thin films, including the one used in this study.

Typically, a small lattice mismatch between the thin film and the substrate is desirable, as a large mismatch could induce dislocations or oxygen vacancies [37]. However, $LaAlO_3$ undergoes a structural phase transition from cubic ($Pm\bar{3}m$) at high temperature to rhombohedral ($R\bar{3}c$) at 544 $°C$ [38]. This transition can be seen through the change of heat capacity in Figure 5.2(a).

During the structural phase transition, LAO switches from a single crystal to a collection of twin domains (see Figure 5.2(b)). For a crystal oriented (001), LAO develops mainly twin domains (100) and (110) [40]. The intersection of (100) and (110) is stress-free for the LAO substrate but can still affect any thin film on top because of the change in the crystallographic axis. The intersection of other domains, such as (100) and (010) is incompatible and builds stress that can lead to the formation of twin needles and strain-induced birefringence near the boundaries [39]. As strain affects the transition temperature of our thin film, it will be important to keep this type of strain landscape in mind from the substrate.

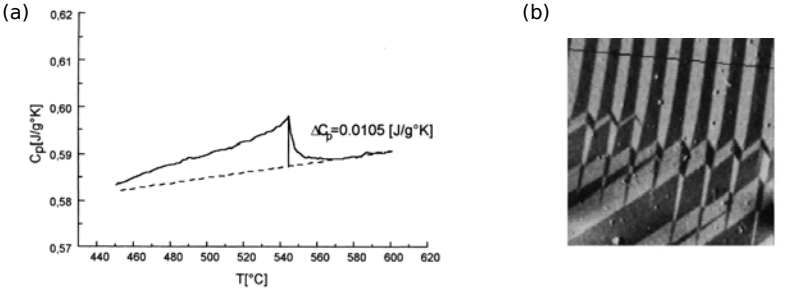

Figure 5.2: a) Excess heat capacity of $LaAlO_3$ near the phase transition from . No discontinuity was observed. b) Scanning force microscopy image of an array of twin domain. Figures from Ref. [39].

5.3 Far-field reflectivity measurement

Reflectivity spectra in the mid-infrared range were measured at various temperatures across the IMT using an FT-IR microscope (Bruker Hyperion 2000 / Bruker Vertex 70) equipped with a helium-flow cryostat (CryoVac Konti Micro). The infrared focal point used in the s-SNOM measurements had a size of approximately (10-15 μm). The spectra at selected temperatures for the cooling and warming stages are shown in Figure 5.3. The temperature dependence of the reflectivity at 939 cm^{-1} (the frequency used in the s-SNOM experiment) is shown in Figure 5.1(c). One can see that the IMT when cooling down is sharper than that at the warming up, which correlates with the temperature dependence of the DC resistivity (figure 5.1(b)).

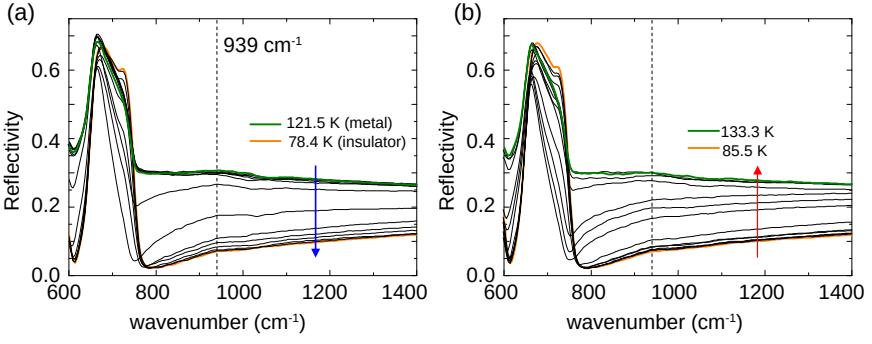

Figure 5.3: Farfield reflectivity measurements of the NNO(10 nm)/LAO sample. (a) and (b), Fourier transform infrared (FTIR) reflectivity spectra at several temperatures across the IMT during the cooling down (a) and the warming up (b). The vertical line denotes the frequency used in the s-SNOM experiment (940 cm^{-1}).

Using Reffit and the Drude-Lorentz formula 5.1, the dielectric function in table 5.1 is obtained:

$$\epsilon(\omega) = \epsilon_\infty + \sum_j \frac{\omega_{p,j}^2}{\omega_j^2 - \omega^2 - i\gamma_j\omega} \ . \tag{5.1}$$

This set of measurements is valuable for predicting the s-SNOM signal across the transition. As shown in Table 5.1, the plasma frequency of the Drude contribution begins at a lower frequency than the illuminating wavelength in the insulating state, but exceeds it in the metallic state. During the transition, we expect the plasma frequency to match the s-SNOM illuminating wavelength, leading to absorption. Since the s-SNOM technique couples an oscillating dipole to the sample surface, any absorption will cause an increase in the phase of the s-SNOM signal, analogous to how friction increases the mechanical phase in AFM.

	ϵ_∞	$\omega_{p,j}$	ω_j	γ_j
LAO	3.83	689.71	189.71	2.00
		853.62	429.19	2.00
		359.94	652.65	18.58
NNO (metal)	11.7	24024	888.38	4181.8
		15136	0	174
		35565	24700	40412
NNO (insulator)	1.39	25292	3995.7	3275
		760.3	0	179.5
		35565	24700	40412

Table 5.1: Dielectric function of the LAO, metallic NNO and insulating NNO in the unit of cm^{-1} obtained by fitting the reflectivity from data in Figure 5.3

This prediction can be further validated by examining the Fresnel coefficient across the phase transition. Due to the large spot size of the reflectivity measurement (50 μm) and the anticipated inhomogeneous state during the phase transition, we are unable to directly calculate the dielectric function of NNO within the hysteresis region. Instead, we linearly interpolate the dielectric function between the metallic and insulating states, using the parameter f, where $f = 1$ represents the purely metallic state and $f = 0$ corresponds to the insulating state. Using the geometry of our experiment (Equation 3.7), we can plot the Fresnel coefficient for different values of f (Figures 5.4(a-d)) to reproduce the phase transition.

Plotting the imaginary part of the Fresnel coefficient for different values of metallicity f reveals a polariton branch (Figure 5.4(a)) that originates at low frequency ($\omega_{\mathrm{phonon}} = 700\,\mathrm{cm}^{-1}$) in the insulating state. This branch

hybridizes with the LAO plasmon and intersects the experimental parameters ($q_{\text{opt}} = \frac{1}{r_{tip}} = 2.5 \times 10^5\,\text{cm}^{-1}$ and $\omega_{\text{exp}} = 940\,\text{cm}^{-1}$) for intermediate metallicity ($f = 0.12$, Figure 5.4(b)). In the metallic state, this branch lies at a momentum much lower than the experimental one (Figure 5.4(c)).

To better align with experimental results, Figure 5.4(d) focuses on the evolution of r_p (real and imaginary) as a function of f for the q and ω matching the experimental parameters q_{opt} and ω_{exp}. Using Equation 4.43, this simple graph provides a useful starting point for predicting the local signal detected by the s-SNOM technique throughout the transition.

Figures 5.4(d) and 5.4(e) provide a comparison of the simple quantity r_p (shown in 5.4(d)) with the point dipole model and the static dipole, represented by the solid and dashed lines in Figure 5.4(e), respectively and presented in section 4.3 and 4.3.1 respectively. All three curves display qualitatively the same behavior with a phase maximum at low metallicity and an increase in amplitude during the IMT. The last panel of Figure 5.4 displays the curves shown in panel (e), but in the form of an amplitude-phase correlation. This type of plot will be valuable later, as SPs manifest as a clockwise spiral [41].

5.4 Experimental setup

Figure 5.5 sketches our experimental setup. The illumination wavelength is fixed at 939 cm^{-1} for all measurements presented in this chapter. This energy is chosen to give a high near-field contrast between the metallic and insulating phases of NNO because the optical signal is expected to follow the Drude response. The detection scheme used is the pseudo-heterodyne detection. In order to avoid the indirect illumination artifacts (figure 5.5(b)), we are presenting the ratio of the third harmonic divided by the second. Mester et al. [33] demonstrated that this ratio remains unaffected by variations in illumination intensity. An inhomogeneous sample would introduce indirect illumination of the tip, with the intensity depending on the tip's position. More importantly, this variation could occur over distances larger than the diffraction limit. To avoid this effect, we will take signal of the form: $s_n e^{i\phi_n}$ with n the harmonic number, we will present $s_r = \frac{s_3^{\text{sample}}/s_2^{\text{sample}}}{s_3^{\text{ref}}/s_2^{\text{ref}}}$ for the amplitude and $\phi_r = \phi_3^{\text{sample}} - \phi_2^{\text{sample}} - (\phi_3^{\text{ref}} - \phi_2^{\text{ref}})$ normalized by the signal on gold.

We expect the amplitude signal to be a straightforward marker of the phase of NNO, with a high signal for the metallic state and a low for the insulating. The spatial resolution of the near field signal is the same as the one for the AFM measurement and is fixed by the AFM tip size ≈ 50 nm.

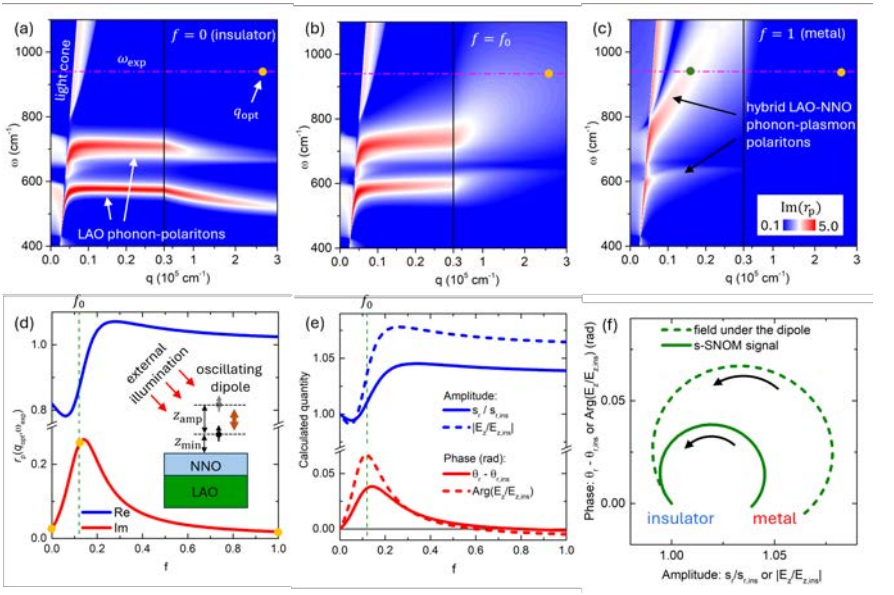

Figure 5.4: Calculated SP dispersion and s-SNOM signal far from boundaries as a function of the metallicity parameter f of the film. (a-c) Frequency-momentum maps of $\mathrm{Im}(r_p)$ for $f = 0$ (insulator), 0.12 (f_0) and 1 (metal). The brown circles indicate the values of $q_{\mathrm{opt}} = 2.5 \times 10^5$ cm^{-1} and $\omega_{\mathrm{exp}} = 940$ cm^{-1}. Note the horizontal scale change at $q = 0.3 \times 10^5$ cm^{-1} marked by vertical lines. The green circle in (c) indicates the SP momentum in the metallic state at ω_{exp} (d) Real and imaginary parts of Fresnel reflection coefficient $r_p(q = q_{\mathrm{opt}}, \omega = \omega_{\mathrm{exp}})$ as a function of f. (e) insulator-normalized amplitude $s_r/s_{r,\mathrm{ins}}$ (solid blue line) and phase $\theta_r - \theta_{r,\mathrm{ins}}$ (solid red line) of the complex-valued 3rd to 2nd s-SNOM harmonics ratio far from edges calculated using the oscillating point-dipole model (the schematics is shown in the inset of panel d). The dashed lines are the E_z field below a static dipole (field-below-dipole approximation of the s-SNOM signal). The data are normalized with respect to the insulator state. (f) Amplitude-phase characteristics to both complex quantities shown in panels (d) and (e).

5.5 SNOM signal through the IMT

Focusing initially on the near-field amplitude, Figure 5.6 shows the evolution of the phase transition during both warming and cooling processes. In Figures 5.6 (a), (c), and (d), we observe that the transition occurs more abruptly during cooling than warming, consistent with the results from Figure 5.1 (b) and (c).

Before proceeding, it is important to note that the sample consists of two distinct NNO regions, each with different transition temperatures. Region A, shown in Figure 5.6(a), undergoes its phase transition 5 K lower than region B during both warming and cooling. This temperature difference can be attributed to the distinct morphologies of the two regions, as seen more

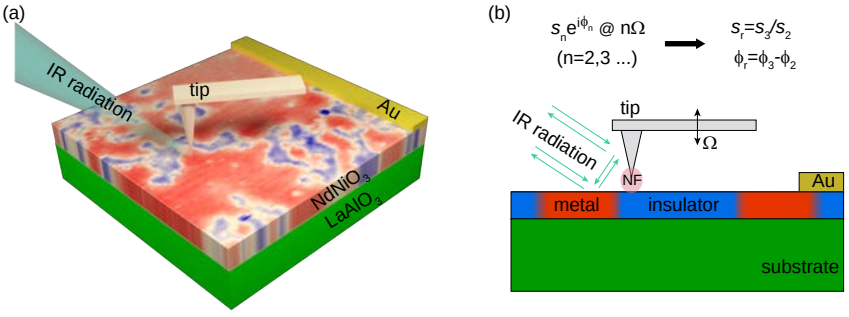

Figure 5.5: Nano-infrared imaging of IMT of NNO film on LAO substrate. (a) Schematics of s-SNOM measurements, where a metallic tip illuminated by infrared laser scans across the sample surface. Au/Pt stripe of around 40 nm thick was deposited on the sample surface, acting as a reference for near-field signals. (b) Side view of the experimental configuration. The tip is illuminated directly by the infrared laser and indirectly by far-field scattering at the sample surface. Complex-valued near-field signals $s_n e^{i\phi_n}$ were obtained by demodulating at different harmonics $n\Omega$ (n=2,3,$\cdots$), where Ω is the tip oscillation frequency. The ratio between near-field signals of the third and second harmonics is adopted to eliminate the influence of far-field scattering.

clearly in Figure 5.6(b). Region A exhibits regular terraces, while region B is more irregular. This morphological difference is likely responsible for the variation in transition temperature. The irregular morphology of region B suggests a higher defect density, which may relax the strain imposed on the NNO by the LAO substrate, restoring a transition temperature closer to the bulk one. Additionally, the morphology of region B may be influenced by incomplete terraces on the LAO substrate, as observed in previous studies [42].

The region A is covering most ($> 95\%$) of the surface of our sample. The LAO terraces can be visible in the A region at 109 and 114 K. Similar observations were done by G. Mattoni et al. [43] where they grow a thin film of NNO on top of $NdGaO_3$. Despite a different strain from the substrate ($+1,4\%$ compared to -0.5% for LAO) and a different imaging technique (photoemission electron microscopy), they also observe that the mixed state is composed of domains aligned with the atomic terraces of the substrate.

During a transition, because of inhomogeneous strain, we expect the transition temperature to vary spatially in the thin film. If no stiffness of the order parameter were present ($\zeta = 0$), each part of the sample would switch at its preferred temperature as it would be independent of its neighbors.

To explain the difference in speed of the cooling down and warming up, one can look at Equation 2.7. The minima of the free energy corresponding to the insulating state is moving away from zero as we lower the temperature.

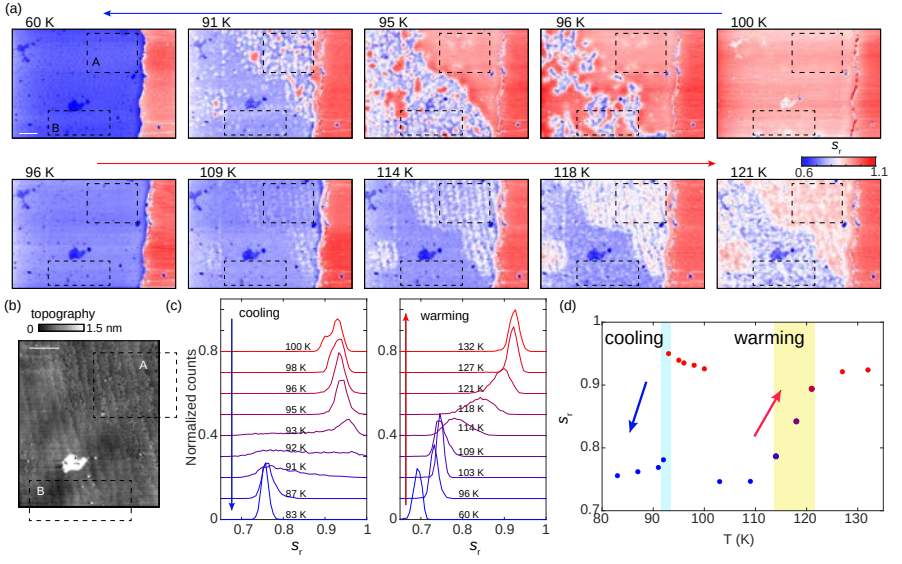

Figure 5.6: Measured near-field amplitude signals on the NNO (10 nm)/LAO sample at 939 cm^{-1}. (a) Images of s_r during cooling and warming processes. Two regions A and B with different transition temperatures are marked. (b) The corresponding topography image was obtained at room temperature. Here the atomic terraces from LAO are artificially flattened to show the morphology difference between regions A and B. (c) Distribution histograms of s_r for the cooling (left) and warming (right) process for the region A. (d) Temperature-dependent evolution of the peak positions of s_r for the cooling and warming process. Scale bars, 2 μm.

This means that the energy cost of a domain barrier between metal and insulator, due to the ζ term in the free energy, is lower during the metal-to-insulator transition compared to the insulator-to-metal transition since the former happens at a higher temperature than the later.

During the cooling, big areas of the sample synchronize their switching to the insulator state. In doing so, the stiffness cost is paid only at the edge of those domains. This is compatible with the histogram in Figure 5.6(c), where the transition is abrupt in temperature.

During the warming, the picture is much more nuanced. The histogram shows intermediate values of the near field amplitude, despite a lower sampling in temperature than in the cooling. We can see that the system, with the stiffness cost lowered in the warming up, favors respecting the local transition temperature. This explains why the atomic terraces, varying the local strain, are visible during the warming up and not the cooling down. With this effect in mind, we can partially explain the dichotomy seen in Figure 5.6 between the warming up and cooling down.

Looking at Figure 5.7, we can see that the near-field phase paints an

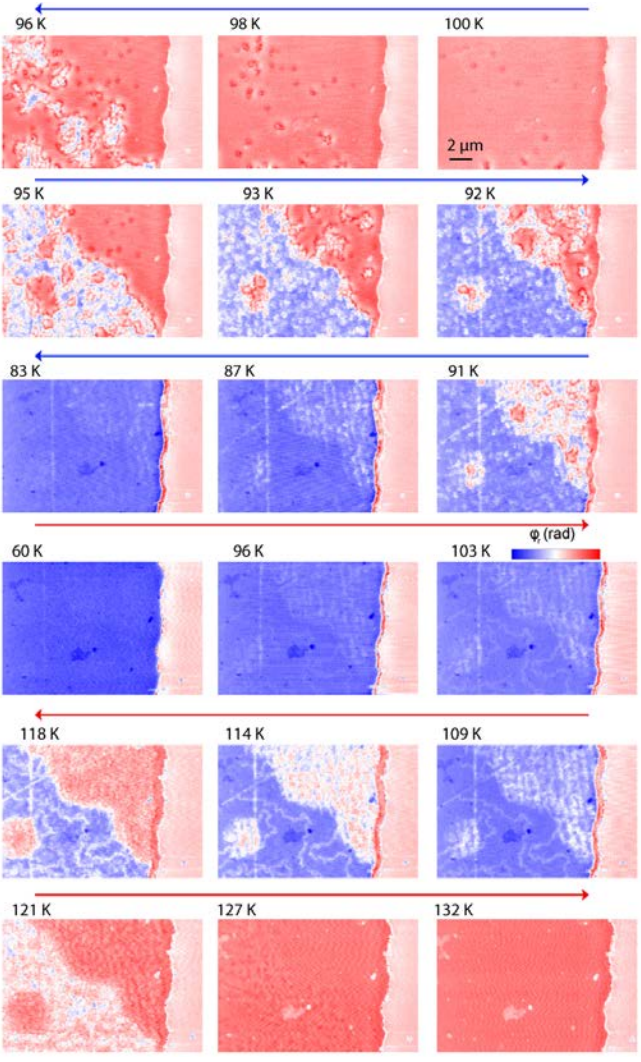

Figure 5.7: Measured near-field phase signals on the NNO (10 nm)/LAO sample at 939 cm^{-1} across the phase transition. Scale bar, 2 μm. The blue arrow on top indicate a cooling down and the red one indicate a warming up.

even richer picture of the transition than the near-field amplitude. The overall trend is similar to the near-field amplitude with a lower near-field phase in the insulating phase compared to the metallic one. The dichotomy between warming up and cooling down is also present with sudden and sharp nucleation during the cooling and a more gradual transition during the warming up. During the cooling down, a small increase of the near-field is

visible, hinting at the area where the insulating phase nucleation is starting. This small increase in the near-field phase precedes any amplitude variation, as can be seen in Figure 5.7 at 100 K.

One can see in Figure 5.7 at 96 K that the phase signal has the tendency to increase close to a metal-to-insulator boundary. This behavior is in accordance with the Figure 5.4(b) where a phase maximum occurs during the transition, in contrast to the amplitude signal, which evolves smoothly.

Additional features revealed by the near-field phase are best visible at 114 K in Figure 5.7. We can see two straight lines of high-phase signal (in white) crossing at approximately 45 degrees over the insulating state (in blue). Because of their angle of crossing, we attribute them to twin boundaries of the LAO substrate [44], causing a local strain that slightly lowers the transition temperature. At the same temperature, we can also see an irregular frontier (in white) in the insulating part of the sample. These structures, contrary to the straight line caused by the twin boundary in LAO, appear only during the warming-up process. They were studied in [45] and identified as the boundary of domains of an opposed sign of the magnetic order parameter. In our case, we identify these boundaries as domain walls (DW) between two insulating nucleation centers growing and coming into contact with each other. The pattern done by these boundaries is unique to each cool-down and is completely erased when the sample is warmed up to the metallic phase. The next section focuses on explaining the evolution of these boundaries.

5.6 Ginzburg-Landau simulation

The difference in the cooling down and warming up transition is quite striking. To explain this difference, we must go back to Equation 2.9 and determine the four parameters. With the substitution $f = f'(2/9)|b|^3c^{-2}$, $a_0 = a_0'(2/3)b^2c^{-1}$, $\Phi = \Phi' b'^{1/2} 3c^{-1/2}$ and $\zeta = \zeta'(2/3)^{-1/2}|b|c^{-1/2}$, we can simplify the formula to:

$$F'(\Phi', T) = \frac{1}{S}\iint a_0'(T-T^*)\Phi'^2 - \frac{\Phi'^4}{2} + \frac{\Phi'^6}{6} + \frac{\zeta'^2}{2}\left[\left(\frac{\partial\Phi'}{\partial x}\right)^2 + \left(\frac{\partial\Phi'}{\partial y}\right)^2\right] dxdy. \tag{5.2}$$

We will later drop the prime sign. This substitution removes two parameters, but prevent us to use the fluctuation-dissipation theorem as we are no longer working with the free energy. The parameters λ and ν are now independent in the Langevin Equation 2.19 and have to be fitted. Two parameters are still to be determined: a_0 and ζ. The first one can be determined using the relation 2.7. We get: $a_0 = \frac{1}{2(T^{**}-T^*)}$ where T^* and T^{**} are respectively the upper and lower temperature limit of the hysteresis. In our case, the hysteresis spans

over 25 K which gives us $a_0 = 0.02\ \mathrm{K}^{-1}$. The last parameter, ζ, controls the energy cost of spatial inhomogeneity of the order parameter. Measurements conducted by Dominguez et al. [46], where $SmNiO_3$ and $NdNiO_3$ were stacked periodically (see Figure 5.8(a)), enable us to determine ζ. The two materials have different phase transition temperatures: 352 K for $SmNiO_3$ and 100 K for $NdNiO_3$. For low enough superlattice length (6 nm), they observe the two transitions merging to one temperature (see Figure 5.8(b)). By assuming the same ζ parameter in the two materials, we conclude that $\zeta = 1.5$ nm.

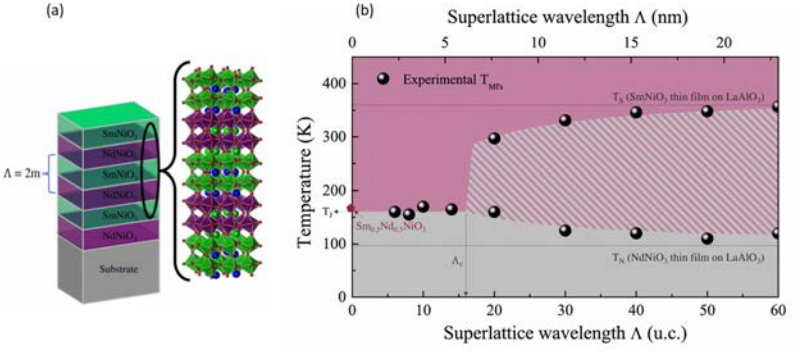

Figure 5.8: (a) superlattices composed of $SmNiO_3$ and $NdNiO_3$. (b) Transition temperatures of the superlattice as a function of the superlattice periodicity. Adapted from Ref. [46].

In our case, the transition is of the first order and happens in a thin film (10 nm thick). In this case, we will allow inhomogeneity of the transition temperature in the plan of the film (x and y) but not along the z-axis. To focus on the effect of local strain on the transition temperature, we force the order parameter to remain positive in the first simulation to forbid the formation of Ising wall and we introduce local variation of the transition temperature. In the second simulation, we fix a constant transition temperature over the sample but put no constrain on the sign of the order parameter to simulate Ising domain wall.

Figure 5.9 (a) shows the evolution of the free energy across the IMT. Figure 5.9 (b) represent the behavior of the order parameter across the IMT of a fully homogeneous sample. Figure 5.9 (c) plot the evolution of three key energies: the energy of the metallic state, the insulating state and the energy barrier between them that vanish outside the transition temperature range (T^* to T^{**}). Figure 5.9(d) mimics our experiment with a local variation of T^* in the form of vertical lines having the phase transition 5 K lower than the rest of the simulation. We indeed recover the behavior of the experiment with the sudden transition during the cooling down,

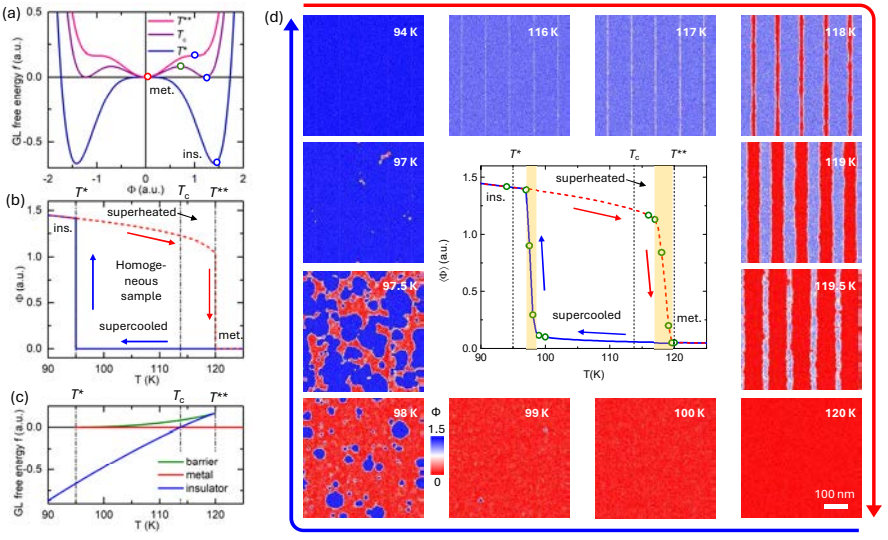

Figure 5.9: (a), dependence of the GL free energy f from Eq. (2) on the order parameter at three characteristics temperatures T^* , T_c and T^{**} . (b), thermal hysteresis of the order parameter in a homogeneous system without thermal fluctuations. (c), temperature dependence of the free energy corresponding to the barrier (maximum), metal (Φ= 0) and insulator ($\Phi = \Phi_0$). (d) Numerical simulation of the evolution of the order parameter distribution in a cooling-warming cycle, where the transition temperature T = 95 K everywhere, apart from the minority regions forming narrow (2.5 nm) periodic stripes separated by 100 nm, where it is set to 90 K. The formation of the Ising walls is suppressed artificially by only accepting positive value of Φ. In the center, the hysteresis of the spatially averaged order parameter is shown. The shaded regions indicate thermal width of the metal-to-insulator and insulator-to-metal transitions.

visible both in a sharp increase of Φ with the temperature lowering and also visible in insulating domains nucleating regardless of the local transition temperature. The difference in local transition temperature is visible only in the warming-up transition.

Figure 5.10(d) simulates a thermal cycle with the presence of Ising DW. The order parameter has to cross zero at DW, creating a closed metallic ribbon. Figure 5.10(c) shows an increase in the thickness of those metallic ribbons with the temperature with divergence at T_c. Above this temperature, the DW walls expand to cover the whole surface as for low temperatures, the DW are small enough to be not resolved by s-SNOM. The DW profile is described as [47]:

$$\Phi(x) = \frac{\Phi_0 \sinh(\frac{x}{w})}{\sqrt{A + \sinh^2(\frac{x}{w})}} \tag{5.3}$$

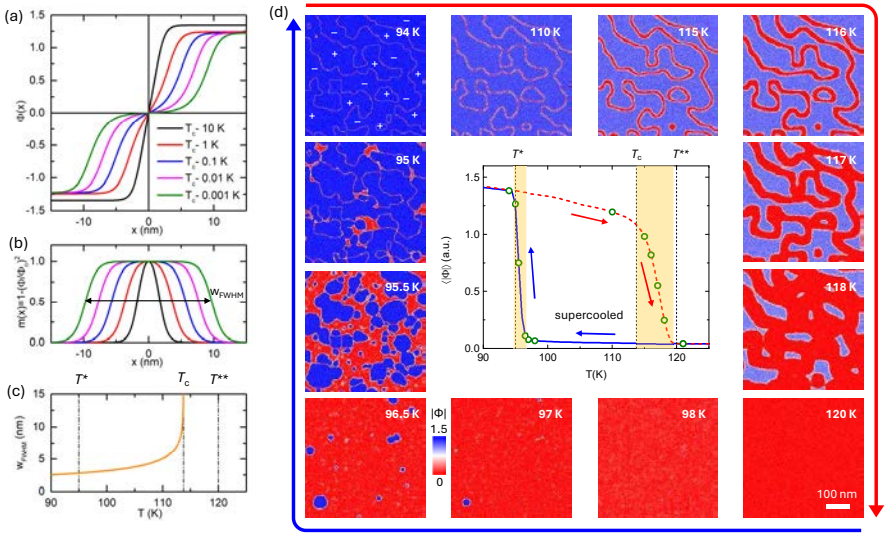

Figure 5.10: (a) Temperature evolution of the equilibrium profiles of the order parameter $\Phi(x)$ across the Ising domain wall. Above T_c, the DW are unstable. (b) The metallicity function $m(x) = 1 - \Phi(x)^2/\Phi_0(x)^2$ corresponding to the solutions in panel (a). Definition of the FWHM width of the DW region, full width at half maximum (FWHM) is shown with the arrow. (c) theoretical temperature dependence of FWHM.(d) Numerical simulation of the evolution of the order parameter distribution in a cooling-warming cycle, where the transition temperature $T^* = 95$ K everywhere, but the formation of the Ising domain walls is not artificially suppressed. In the center, the hysteresis of the spatially averaged order parameter is shown. The shaded regions indicate the thermal width of the metal-to-insulator and insulator-to-metal transitions.

with $A = \frac{3c\Phi_0^2+b}{2c\Phi_0^2+b}$ and $w = \frac{\zeta}{\Phi_0^2\sqrt{6c\Phi_0^2+2b}}$. The variable b and c being -1/2 and 1/6 in our case.

The existence of those DW paints a different story for the insulator-to-metal and the metal-to-insulator transition. The insulating phase at low temperatures will most likely always contain those metallic closed ribbons that expand during the transition. In contrast, the high-temperature metallic phase has no reason to contain any insulating area. These differences bring asymmetry to the transition. The metal-to-insulator transition has to pay an extra boundary energy cost when the insulating phase nucleates inside a metallic sample. The insulator-to-metal has this boundary cost already paid in the form of those DW, leading to a more gradual transition as those DW expand. This difference can be seen both in measurement (figure 5.6(c)) and simulation (figure 5.10(d)). The excellent correspondence between experiment and simulation leads us to believe that we successfully captured

key parameters of the transition process.

5.7 Surface and edge polariton at the insulator-metal boundary

Figure 5.11(a) shows a line profile of the amplitude (s_r) and phase (ϕ_r) through an insulator-to-metal boundary at 95 K during the cooling down. For both amplitude and phase, the near-field signal does not evolve monotonically through the phase boundary. Going from the insulating phase to the metallic one, we have a sharp peak followed by a dip for the near-field phase and a wide peak at the boundary for the near-field amplitude. The discrepancy between the measurements and Figure 5.4(d-f) can be attributed to the fact that Figure 5.4 was calculated based on the assumption of only local effects, disregarding the polariton interference pattern.

Plotting the near-field phase as a function of near-field amplitude in Figure 5.11(b) reveals a spiral shape quite similar to spirals observed in [41] of damped plasmon polariton.

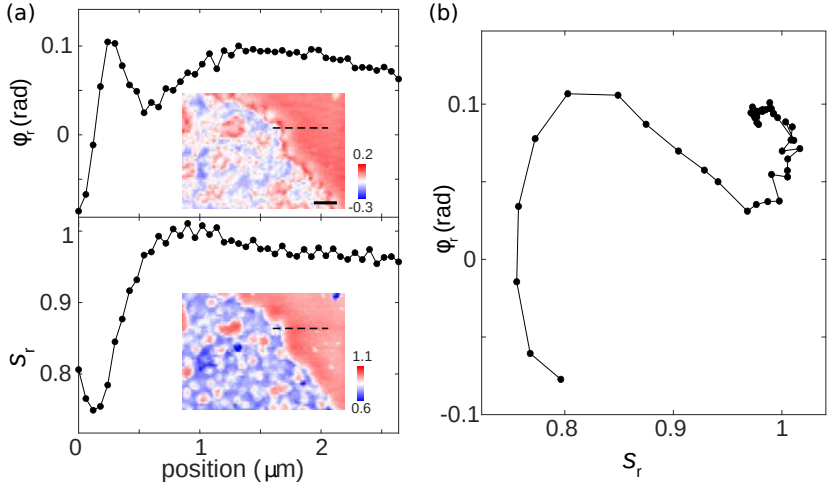

Figure 5.11: Evolution of the near-field signal trough the IMT. (a) Extracted profiles of ϕ_r and s_r across the boundary between the metallic and insulating phase (dashed lines in the inset images) at 95 K during cooling. The insets are the corresponding near-field images. (b) Corresponding correlation curve between the near-field amplitude and phase signals.

The difficulty in analyzing the plasmon response in the profile line in Figure 5.11 resides in the fact that the launcher, the insulator-to-metal

boundary, is not spatially sharp. In the case of a punctual boundary ($s = 0$), the field evolves spatially as [41]:

$$E_z(x) = E_{z,l} + rE_0 \frac{e^{i(q'+iq'')x}}{\sqrt{x}} \tag{5.4}$$

for $x > 0$, with $E_z(x)$ the total detected field, $E_{z,l}$ the field of the local factor and $rE_0 \frac{e^{i(q'+iq'')x}}{\sqrt{x}}$ the field of the plasmon. r represent the reflection coefficient of the boundary and $q' + iq''$ is the complex wavevector of the plasmon wave.

As our boundary is more complicated, we used three-dimensional electromagnetic simulations (COMSOL Multiphysics) to calculate the near-field response of different boundary geometry. Figure 5.12 presents the results of four distinct simulations: two simulations with an insulator-to-metal boundary of 1 µm thickness (shown in the first column of Figure 5.12), and two simulations with a boundary thickness of 0 μm. An additional parameter explored in these simulations is the height of the dipole. The first two rows of Figure 5.12 feature a dipole placed at a height of 200 nm, while the third row displays a dipole positioned at 1.5 μm. Altering the dipole height effectively changes the momentum of the probed response, with a higher dipole corresponding to lower momentum (see Equation 4.47). Simulations with a dipole height of up to 1.5 µm matches better the momentum of the hybrid phonon-plasmon polariton branch depicted in Figure 5.4(c).

The four simulations shown in Figure 5.12(a,b,i,j) are color-coded as follows: red curves represent the near-field phase, blue curves represent the amplitude, and the black dash-dotted lines correspond to the purely local factor. This local signal was simulated using a homogeneous sample with the corresponding metallicity, removing the presence of scatterers or reflectors. Any deviation between the blue/red curves and the black dash-dotted line can thus be attributed to polariton behavior.

In Figure 5.12(a), the near-field signal closely matches the local value. This can be explained by the low position of the dipole, which results in a high momentum that is insufficient to excite SPs. Referring to Figure 5.4(c), the optimal momentum for launching polaritons is 0.15×10^5 cm^{-1} (indicated by the green point). In the case of the simulation in Figure 5.12(a), the probed momentum is 0.4×10^5 cm^{-1}, which is too high to excite polaritons, and as a result, the signal is dominated by the local dielectric function.

This is not the case in Figure 5.12(i), where the dipole is positioned higher, resulting in a lower momentum (0.07×10^5 cm^{-1}) that better matches the momentum of the SP at the illuminated energy. The excitation of SPs leads to a discrepancy between the near-field signal and the purely local signal at the boundary and on the metallic side of it. Due to high damping,

instead of observing an interference pattern with a fixed spatial frequency and multiple oscillations, we observe a single overdamped oscillation on the metallic side at a distance from the boundary of approximately the optimal momentum of the polariton branch (0.7 μm).

A distinct non-local effect is observed in Figure 5.12(b), this time in the immediate vicinity of the sharp boundary. The in-plane map of the out-of-plane electric field intensity shown in Figure 5.12(e) reveals the presence of an edge polariton (EP). This edge state propagates along the sharp boundary and primarily manifests as an increase in the near-field phase (dissipation) as the dipole launches it.

Figure 5.12(f) presents the profile of this EP for varying boundary thicknesses. The trend shows that both the sharpness and intensity of the EP increase with the sharpness of the boundary. Interestingly, the EP remains detectable, albeit weakly, even for boundaries as large as one micrometer. Figure 5.12(j) is presenting both a low dipole and and a sharp boundary, resulting in the formation of both surface and edge polaritons. All the curves are compiled into amplitude-phase correlation curves, shown in Figure 5.12(c,k) for the low and high dipoles, respectively. The deviations from the local curves are identified either as SP (clockwise spiral) or EP.

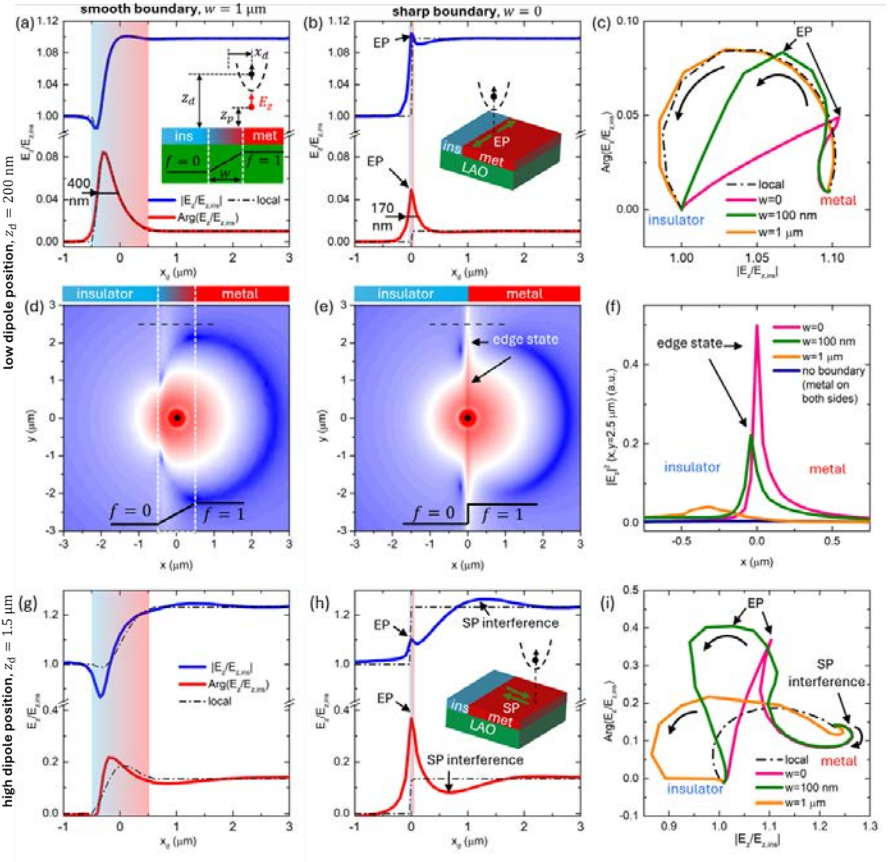

Figure 5.12: Numerical simulation of the s-SNOM signal across metal-insulator boundaries of various widths. (a) and (b), amplitude (blue) and phase (red) of the probe-point field E_z calculated on a smooth boundary (a) and a sharp boundary (b) as a function of the dipole position x_d with respect to the center of the edge. The dipole height z_d is 200 nm. For comparison, the dashed-dotted lines represent the corresponding values calculated far from edges on a sample with a uniform metallicity equal to the local value $f(x_d)$. (c) Amplitude-phase correlation curves for the sharp (w=0), intermediate (w=100 nm) and smooth (w = 1 μm) boundaries compared with the local curve (dashed-dotted line). (d) and (e) the xy map of the electric field, $|E_z(x, y, z)|^2$, at the level z = 25 nm above the surface, when the dipole emitter is located at the above the smooth and the sharp boundary (x_d=0, z_d = 200 nm). (f) field profiles along the dashed line in panels (d) and (e) for the sharp, intermediate and smooth boundaries as well as for a uniform metallic sample without boundaries. (g-i), the same as (a-c), but for a high dipole position z_d = 1.5 μm. The insets in (a) and (b) describe the calculation geometry and depict the excitation of the EP and SP by the tip. In all simulations z_p = 25 nm.

CHAPTER 6

Current driven IMT

The IMT can be achieved using different parameters such as temperature, doping and high pressure [48]. An electric current can also trigger the transition via Joule heating [49]. In the last case, the transition takes the form of a volatile percolative metallic filament. Possible applications range from neuromorphic computing [50–56] and probabilistic bits for stochastic computing [57–59] to serve as electro-optical switches for optoelectronics [60–64]. A better understanding of electrically induced IMT is still necessary before practical applications. In this chapter, we will focus on studying the length scale of the electrically induced filaments, the effect of the resistivity drop from insulator to metal as well as the sharpness of the switch. This chapter is adapted from reference [4].

6.1 Sample preparation

The samples used were thin films (40 nm thick) of $NdNiO_3$ or $SmNiO_3$ on oriented (001) $LaAlO_3$ substrates. Electrically isolated areas were defined using etching and optical lithography (in Figure 6.1(b)). Platinum electrodes were deposited using optical lithography and sputtering. The results are two-terminal micro-devices composed of two platinum electrodes separated by a thin film of $NdNiO_3$ or $SmNiO_3$. The IMT can be triggered electrically and be detected electrically or optically (SNOM or optical microscope). The imaging is done *in operando* i.e with an applied current to observe the percolating filament.

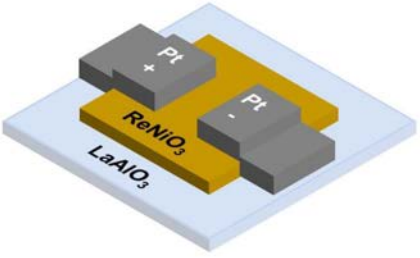

Figure 6.1: Schematic representation of the two-terminal devices. Nickelate islands (brown) were patterned on top of $LaAlO_3$ substrate (blue). Two platinum electrodes (gray) were used to trigger the IMT electrically. The schematic is not to scale. Figure and caption adapted from Ref. [4].

6.2 Visible optical microscopy result

Figure 6.2 shows a metallic filament formation and its effect on the voltage-current (V-I) curve. The micro-device is $NdNiO_3$ at a temperature below the IMT (60K). The V-I curve in the central panel of Figure 6.2 can be decomposed into three regimes. In the first regime, below 5 mA, the device is insulating and has a slowly decreasing resistance. Between 5 and 10 mA, a metallic filament is formed, when ramping up the current, and the resistance of the device drops. Above 10 mA, the resistance is slowly increasing with the current. The increase in current leads to higher Joule heating of the device.

In Figure 6.3, the same measurement is repeated at different temperatures and different thin film ($NdNiO_3$ in (a) and $SmNiO_3$ in (d)). Both Figures 6.3(a) and (d) display a bigger and sharper resistance drop at low temperature. Both samples, for a given current (20 mA), have the filament width increasing with temperature. This trend can be seen in Figure 6.3(b), (c), (e) and (f) where lower temperature leads to higher current density. When comparing the filament width in $NdNiO_3$ and $SmNiO_3$, we observe that, for a given current, filaments are thinner in $NdNiO_3$.

6.3 Resistor network simulations

Another method to identify the key parameter which determines the filament size is the resistor network simulation [65, 66]. The resistor network simulates our thin film by a two-dimensional node network. Each node corresponds to a region in space on the order of 10 nm. Each node can either be in an insulating state with a decreasing resistivity as temperature increases or be

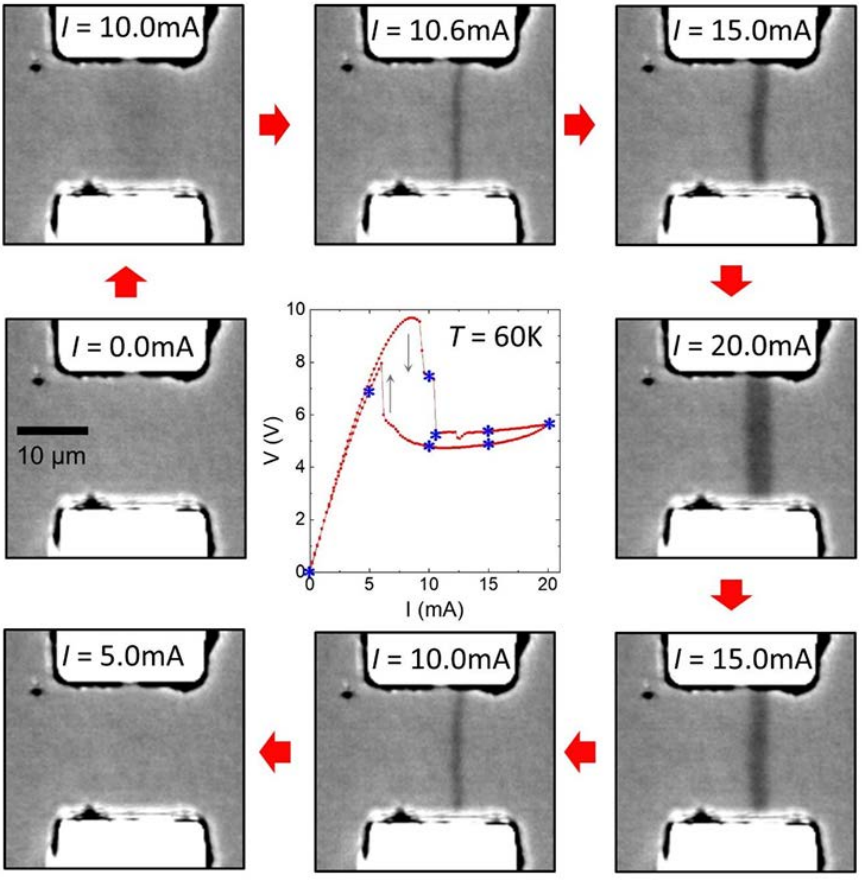

Figure 6.2: Filament size dependence on applied current. The illumination wavelength is 532 nm. Central panel: V-I characteristics of a $NdNiO_3$ micro-device at T = 60 K. Blue asterisks mark currents at which the outer panels were captured. Outer panels: standard optical microscope images of the devices at different applied currents. Figure and caption from Ref. [4].

in a metallic state with constant and low resistivity. The temperature of each node evolves in discrete time steps with the following equation:

$$T_{\mathrm{ij}}(t) = T_{\mathrm{ij}}(t-1) + \frac{P_{\mathrm{ij}}(t)}{C} - \frac{K}{C}\left(5T_{\mathrm{ij}}(t-1) - \sum_{\mathrm{kl}}^{NN} T_{\mathrm{kl}}(t-1) - T_0\right) \quad (6.1)$$

with K the thermal conductivity, C the thermal capacity and the sum with indexes kl runs over the nearest neighbor nodes.

Equation 6.1 contains the Joule's heating between a node and its nearest neighbors as well as the heat dissipation through the neighbor's nodes and

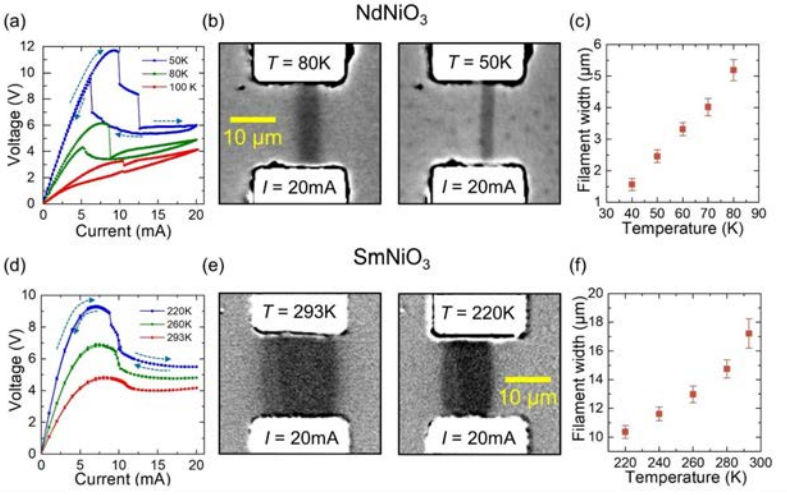

Figure 6.3: Connection between resistive switching properties and filament size. (a), (d) Voltage vs current curves for $NdNiO_3$ and $SmNiO_3$ micro-devices, respectively. Several temperatures are plotted for each material. (b), (e), Wide-field optical microscopy images of filaments in $NdNiO_3$ and $SmNiO_3$, respectively. The current is 20 mA for all four images. The illumination wavelength is 532 nm. Two different temperatures are shown for each material. For the $NdNiO_3$ images, reflectivity was normalized using a region far from the gap. For $SmNiO_3$, differential images are shown, where the reflectivity at I = 0 mA is subtracted at each point. (c), (f), Filament width vs temperature at I = 20 mA. The width was determined using a Gaussian fitting of line scans perpendicular to the filament direction, taking the full-width-half-maximum as filament width. The error bars show the standard deviation of the distribution of widths. Figure and caption from Ref. [4].

the substrate. Once the temperature of a node is determined, it can switch between a metallic and insulating state following an Arrhenius-like law. In this way, each node state is determined by Joule heating and heat dissipation and Joule heating is iteratively determined by each node state.

Figure 6.4(b) shows the same temperature trend as 6.3(a): lower temperatures feature sharper voltage drops. Figure 6.4(c) shows that the filament size increases with temperature in a similar fashion as Figure 6.3(c). Finally, Figure 6.4(d) gives us the temperature within the filament, showing that smaller filaments are hotter than large ones.

6.4 Main result discussion

The key parameter that determines the filament size and switching property seems to be the resistivity difference between the insulating and metallic phases. The trend observed in Figure 6.3(a,c) and (d,f) is the following: a higher device temperature leads to a smaller resistivity drop and a

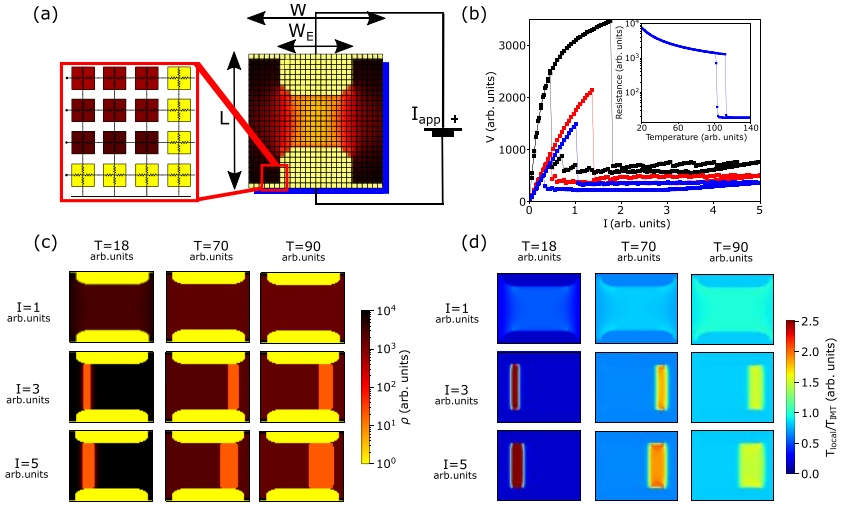

Figure 6.4: Resistor network simulations and current focusing effect. (a) Schematic representation of the simulated resistor network (size W x L). Low resistance electrodes (yellow) define an oxide gap where individual nodes could be either metallic (orange) or insulating (dark brown), as described in the methods section of the supplementary material. (b) Simulated voltage vs. current curves for three different temperatures: 18 a.u. (black), 70 a.u. (red) and 90 a.u. (blue). Inset: Simulated resistance vs. temperature of the device. (c) Simulated, two-dimensional resistivity plots for all combinations of three currents (1, 3 and 5 a.u.), and three device base temperatures (18, 70 and 90 a.u.). Resistivity is plotted in logarithmic color scale. (d) Simulated, two-dimensional temperature plots for all combinations of three currents (1, 3 and 5 a.u.), and three device base temperatures (18, 70 and 90 a.u.). Temperature is plotted in a linear color scale and normalized to the transition temperature (120 a.u.). Figure and caption adapted from Ref. [4].

larger filament width. When comparing $NdNiO_3$ and $SmNiO_3$ resistivity vs temperature curve (figure 1.3), we can see that $NdNiO_3$ has both a sharper resistivity drop and smaller filament width. This observation can be explained as follows: focusing the current in a filament locally increases the temperature and lowers the resistivity at the cost of an increase in resistance due to the geometrical constraint of the filament.

Unfortunately, another property of the device changes with temperature: the thermal conductivity of $LaAlO_3$. It decreases from $0.6 - 0.7$ KW/cm at 60 K to ~ 0.15 KW/cm at 300 K [67]. It means that at low temperatures, the insulating part of the film can better transmit heat to the substrate than the metallic (filament) part of the filament, therefore increasing the sharpness of the filament. When the device temperature close to the IMT temperature (but lower), the contrast of thermal conductivity of the

substrate is less present as the metallic and insulating parts of the film are closer in temperature. The thermal dependence of the thermal conductivity of $LaAlO_3$ also makes the comparison of $NdNiO_3$ and $SmNiO_3$ more difficult.

To isolate the contribution of the resistivity drop during the IMT, we compare the same material and sample with different IMT sharpness. Two $NdNiO_3$ were grown, one with a sharp IMT and one with a gradual IMT. The second film was annealed for 30 minutes at 120 °C in vacuum. The annealing creates oxygen vacancies, reducing the resistivity change across the IMT, as seen in Figure 6.5(a). The annealed film exhibits a lower resistance drop (figure 6.5(b)) and thicker filament compared to the non-annealed one. Additionally, the trend of thinner filament and large voltage drop for big resistance ratio between the metallic and insulating phases is also present in Figure 6.4, where a constant thermal conductivity was used. This confirms that the resistivity change across the IMT is a key parameter controlling resistive switching and filament characteristics, although it does not rule out important contributions from thermal conductivity.

6.5 Scanning near-field optical microscopy result

SNOM measurement is expected to give similar results as the optical microscopy ones but with a higher spatial resolution. All near-field signal displayed in this section will be the ratio of the third harmonic divided by the second for the amplitude (S_r) and the difference between the third harmonic and the second for the phase (ϕ_r) as presented in section 4.3.

Figure 6.6 summarizes the measurement done with the s-SNOM technique. Figure 6.6(a) shows the topography of our device with the $NdNiO_3$ thin film between two platinum electrodes. The topography measurement is taken simultaneously with the near-field signal and is independent of current as the metallic filament does not change the device topography. One can see on the left of Figure 6.6(a) some dust particles (white arrow) that will be present in all near-field measurements. These dust particles appear mostly as a decrease in the near-field amplitude (top line of Figure 6.6(c) and (d)) and do not interact with the filament formation.

The near-field amplitude is a good indication of the metallicity of the material under the AFM tip as a metallic material will give a high polarizability of the couple tip-sample. This effect can be seen in Figure 6.6(c) where the platinum electrodes and mettalic $NdNiO_3$ have a higher near-field amplitude as the insulating $NdNiO_3$.

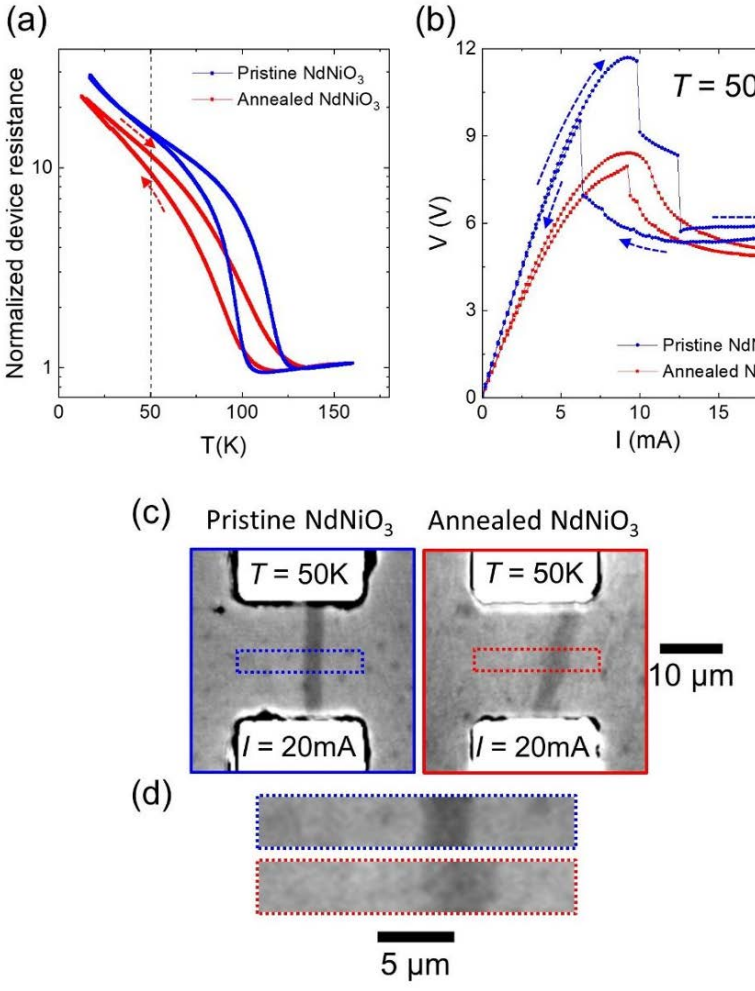

Figure 6.5: Resistive switching and filament characteristics in pristine and annealed $NdNiO_3$. (a) Two probe device resistance vs temperature on pristine (blue) and annealed (red) $NdNiO_3$ films. (b) Voltage vs current at T = 50 K for a pristine (blue) and annealed (red) sample. (c) Wide-field microscopy image of filament formation in pristine (left) and annealed (right) $NdNiO_3$. T = 50 K and I = 20 mA in both cases. Reflectivity was normalized using an area far from the gap region. (d) Zoomed image into the central part of the filament for pristine (top) and annealed (bottom) $NdNiO_3$. T = 50 K and I = 20 mA in both cases. Figure and caption from Ref. [4].

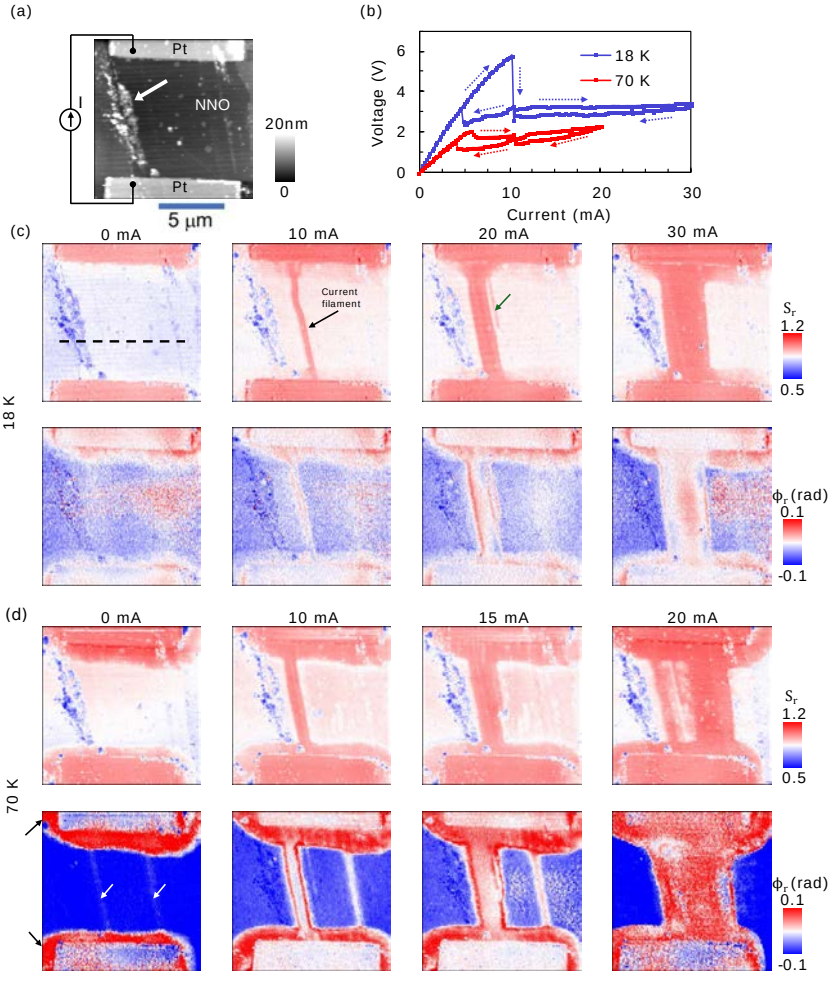

Figure 6.6: (a) Topography of the device with the electrical diagram. The white arrow shows some dust particles on top of the film. (b) Voltage versus current of an $NdNiO_3$ device at low temperature (blue curve) and close to the transition temperature (red curve). SNOM amplitude (S_r) and phase (ϕ_r) at different currents for low temperature (c) and just below the transition temperature (d) at 10000 cm^{-1}. At 0 mA in (d), we see an increase in phase around the electrodes (black arrows) and in two tilted line (white arrows). Current filament is showed in (c) at 10 mA in amplitude and at 20 mA, a green arrow shows a branch in the filament. This last feature is discussed in section 6.5.2. The dotted line in (c) is the position of all line cut of graph 6.7(b-e). It is showed only on one measurement for better readability.

6.5.1 Filament width

A similar trend is observed in s-SNOM and optical microscopy toward the width of the filaments. As in Figure 6.3(a), we find in Figure 6.6(a) that

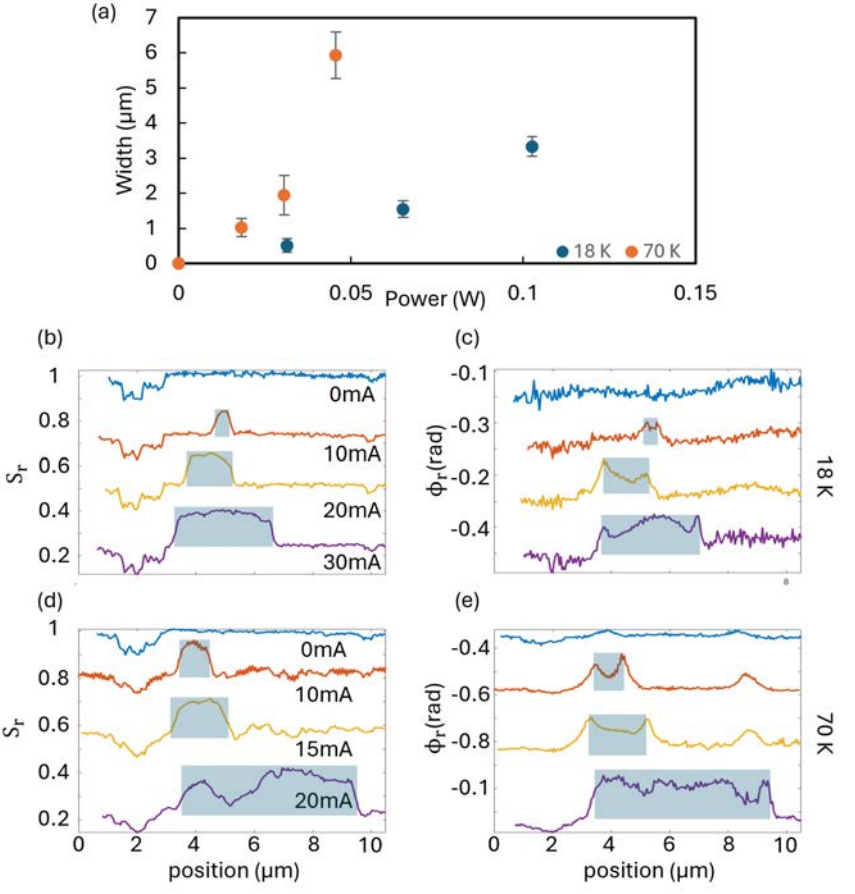

Figure 6.7: (a) Filament width vs power used. The width is taken at half height of the amplitude and is marked by a blue rectangle in (b) and (d). The error bar is equal to the distance taken to the amplitude to reach it's maximum value on the side of a filament. Amplitude cut at 18 K (b) and 70 K (d) and phase cut at 18 K (c) and 70 K (e). The line cut are taken at the position indicated by the dotted line in Figure 6.6(c) for each current and temperature.

larger and sharper resistivity drops are observed at low temperatures. A lower power is needed to trigger the filament formation at 70 K compared to 18 K. This can be understood as the transition occurs at 18 K almost entirely due to the Joule heating. At 70 K, the sample temperature is almost sufficient to trigger the IMT and the Joule heating is the last extra heat that triggers it.

The Figure figure 6.6(c) and (d) also reproduced the result in Figure 6.3(c): for a fixed current, the filament width increases with increasing

temperature. This trend can be seen comparing the filament width between 18 K and 70 K at 10 or 20 mA in Figure 6.6(c) and (d).

The width evolution is summarized in Figure 6.7(a). It can been seen that the spatial sharpness of the filament decreases with increasing temperature. We can see that the evolution of the width with the heating power ($P = U \times I$) is superlinear.

6.5.2 Inhomogeneous strain

The high spatial resolution of s-SNOM reveals new features that escaped or were barely visible with the optical microscopy technique. One of these features is the fact that the filaments are not straight. This is surprising as the shortest path between the electrodes should result in the lowest resistance of the device.

Additional insight can be found in Figure 6.6(c) and (d), where we see that the near-field phase is more sensitive to the IMT and can even be used as a precursor. As seen in Figure 6.6(d), the near-field phase is already increasing in two inclined lines even at zero current where no filament is present (white arrows). One of these lines will host a filament once the transition is done at 10 mA. A possible explanation for this behavior is that the $NdNiO_3$ substrate is applying an inhomogeneous strain to our thin film. The area with the highest strain would have a lower transition temperature [14] and be the starting point for the filament formation.

We believe that this inhomogeneous strain is the origin of the "branch" marked by the green arrow in Figure 6.6(c) at 20 mA. The Joule heating inside the filament can trigger the IMT of a region in contact but not necessarily inside the filament.

6.5.3 Electrode "aura"

Another new feature visible with the s-SNOM technique is what appears to be an aura around the platinum electrodes when the device is close to the IMT temperature (figure 6.6(d) black arrows). This aura manifests as an increase of both near-field amplitude and phase around the electrodes. It indicates that the deposition of the platinum electrode lowers the IMT temperature of the thin film either by inducing strain or chemically. The same aura appears progressively as we increase the current at low temperatures (figure 6.6(c)). This leads to believe that the heat coming from the Joule effect inside the filament allows the region close to the electrode to switch to the metallic phase. At high temperature (70 K in Figure 6.6(d)), this Joule heating is less important since the power used is weaker and the sample is already close to the IMT temperature.

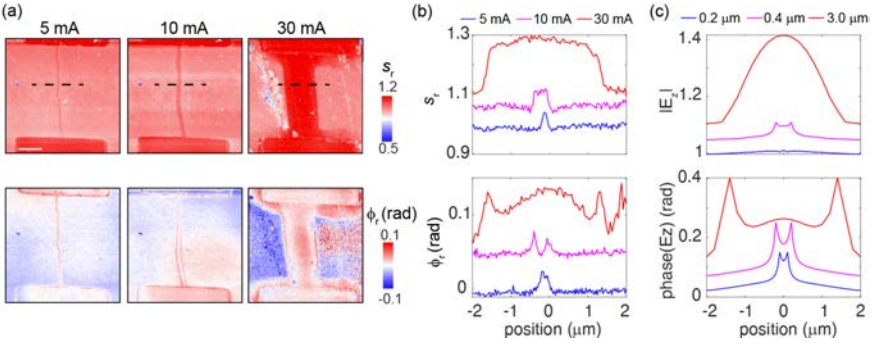

Figure 6.8: (a) Amplitude and phase measurement of filaments at low temperature (18 K) with different currents at 10000 cm^{-1}. (b) line-cuts of the filaments shown in (a). (c) Line-cut of the near-field signal of a two-dimensional model in Comsol with similar geometry as in (b). The Comsol model is discussed in section 4.3.1.

6.5.4 Edge polariton

The last additional feature that the s-SNOM can detect is the maximum of the near-field phase when crossing a filament. This can be better seen in Figure 6.8(b), where the phase is at its highest on the filament's edge. This behavior is well reproduced by a Comsol simulation (model discussed in section 4.3.1) with a similar device geometry (Figure 6.8(c)). This phase increase of the near-field near the filament's edge is similar to the one seen in Figure 5.11(a) at the boundary between the metallic and insulating phase.

The current driven phase transition allows us to realize different phase boundaries thickness. As previously explained, a lower base temperature of the sample results in thinner filaments, due to the significant drop in resistivity and the enhanced thermal conductivity of the LAO substrate, which also leads to sharper boundaries.

This effect is shown in Figure 6.9, where large insulator-to-metal boundaries are observed during the inhomogeneous state close to the transition temperature (panels a-c), or in conducting filaments at temperatures slightly below the transition temperature (panels d-f). Sharp insulator-to-metal boundaries at the edges of conducting filaments are observed at low temperatures (panels g-l). We find that sharp boundaries are linked to higher and more distinct near-field phase peaks, indicative of edge polaritons, consistent with the results shown in Figure 5.12(f) and the analysis of section 5.7.

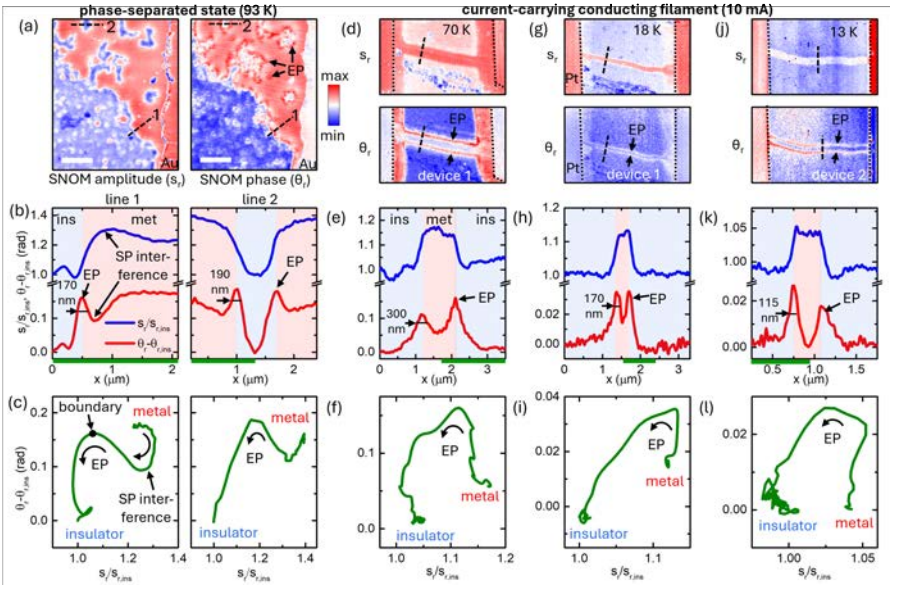

Figure 6.9: s-SNOM mapping of the complex-valued near-field signal in metal-insulator separated $NdNiO_3$ films. Panels (a-c) refer to a inhomogeneous state spontaneously formed close to the transition temperature, while panels (d-l) correspond to the formation of a conducting filament at a base temperature below the transition, as a result of passing a high electric current through the film between two closely separated electrodes and related Joule heating. (a) s-SNOM images of the near amplitude s_r (left) and phase θ_r (right) of a 10 nm thick film at 93 K. (b) insulator-normalized profiles of $s_r/s_{r,\mathrm{ins}}$ (blue) and $\theta_{r,\mathrm{ins}}$ (red) along the two lines 1 (left) and 2 (right) indicated with dashed lines in (a). (c) amplitude-phase correlations (APCs) corresponding to the profiles in (b) taken in the regions marked by horizontal green lines. (d) s-SNOM images of the near amplitude (left) and phase (right) of a 40 nm thick film (device 1) at a base temperature of 70 K, while a current of 10 mA is sent through the film between the two Pt electrodes (marked by dotted lines) separated by 10 μm. The current passes through the spontaneously formed conducting filament, where the local temperature is higher than the transition temperature. (e) Profiles of $s_r/s_{r,\mathrm{ins}}$ (blue) and $\theta_{r,\mathrm{ins}}$ (red) along the dashed line in (d). (f) APC along the same line taken in the regions marked by horizontal green line in panel (e). (g-i) refer to a similar measurement in the same device at 18 K. (j-l) refer to a similar measurement in device 2 at 13 K. The scale bar in (a), (d), (g) and (j) is 2 μm.

CHAPTER 7

Conclusion

In this work, we explored the rich electronic behavior of nickelates through the lens of the s-SNOM. Epitaxial thin films of NNO on LAO were first characterized with X-ray diffraction, transport and reflectivity measurements. The s-SNOM technique was used in both of its main uses: the detection of the local metallicity was used to study the insulator-to-metal transition in the NNO thin film and plasmons reflected of insulator-to-metal boundaries were also detected. The richness of the s-SNOM signal called for careful data analysis to disentangle local and non-local responses, a task that we managed to achieve using Comsol modeling. To consolidate our conclusions and observe the plasmon dispersion, we will in the future measure at different wavelengths (850 to 1700 cm^{-1}).

The IMT was first explored using temperature. The sensitivity of the IMT to the local strain was highlighted by the s-SNOM technique. The spatial resolution of the s-SNOM allowed us to see the effect of the variation of strain due to LAO atomic step and twin boundaries on the local electronic properties of the NNO thin film. An interesting feature was detected in thin irregular and reversible metallic walls in the insulating phase. These walls were already detected in [45] and were described as boundaries of two insulating phases with the order parameter of an opposed sign. Using a back electrode, conductive AFM could be used in the future to investigate the exotic phase of those domain walls.
Using electrical current, we studied the filament formation of the metallic phase. Two key parameters were identified as controlling the width of the

filaments: the resistivity drop during the IMT and the thermal conductivity of the subtract. By comparing a pristine and annealed device, we isolated the contribution of the resistivity drop and demonstrated its importance in the width control.
A promising candidate for future experiment is $La_{0.7}Sr_{0.3}MnO_3$ (LSMO). This material exhibits the reverse transition compared to NNO, being metallic at low temperatures and insulating at high. At low temperatures and with applied voltage, LSMO develops an insulating barrier perpendicular to the current passage [68]. The s-SNOM or conducting AFM technique would increase the spatial resolution of measurements currently done by scanning magneto-optical Kerr effect (MOKE).
At last, we are implementing a strain cell to our setup that will allow us to apply both compressive and tensile strain laterally. With this upgrade, we could study further the coupling between strain and electronics in thin film NNO.

APPENDIX A

Appendices

A.1 List of publications

During the completion of this thesis, the following list of publications has been made by the author:

1. Ruijuan Xu, Iris Crassee *et al.*, "Highly confined epsilon-near-zero and surface phonon polaritons in $SrTiO_3$ membranes", Nature Communications volume 15, Article number: 4743 (2024)

2. Michael Dapolito *et al.*, "Infrared nano-imaging of Dirac magnetoexcitons in graphene", Nat. Nanotechnol. 18, 1409–1415 (2023)

3. Theodor Luibrand, Adrien Bercher, Rodolfo Rocco *et al.*, "Characteristic length scales of the electrically induced insulator-to-metal transition", Phys. Rev. Research 5, 013108 – Published 13 February, 2023

4. Yixi Zhou *et al.*, "Thermal and electrostatic tuning of surface phonon-polaritons in $LaAlO_3/SrTiO_3$ heterostructures", Nature Communications volume 14, Article number: 7686 (2023)

5. Javier Taboada-Gutiérrez *et al.*, "Unveiling the Mechanism of Phonon-Polariton Damping in a-MoO_3", ACS Photonics 2024, 11, 9, 3570–3577

6. Jean-Marie Poumirol *et al.*, "Ultracompact Binary Permanent Rare-Earth Magnet with 1.25-T Center Field and Fast-Decaying Stray Field",

Phys. Rev. Applied 16, 044012 – Published 11 October, 2021

7. Li Geng *et al.*, "Infrared Spectroscopy for Diagnosing Superlattice Minibands in Twisted Bilayer Graphene near the Magic Angle", Nano Lett. 2024, 24, 50, 15956–15963

8. Weiwei Luo, Adrien Bercher *et al.*, "Edge polaritons at metal-insulator boundaries in a phase separated correlated oxide", in preparation

9. Weiwei Luo, Adrien Bercher *et al.*, "Cooling-warming dichotomy of the metal-insulator transition in thin $NdNiO_3$ films", in preparation

A.2 Dipole direct field

From equation 9.18 in [69], the field generated by a dipole $\mathbf{d}$ is:

$$\mathbf{E}(\mathbf{r}) = \frac{e^{iq_0 r}}{r^3}\left(\frac{3 - 3iq_0 r - q_0^2 r^2}{r^2}\mathbf{r}(\mathbf{rd}) - (1 - iq_0 r - q_0^2 r^2)\mathbf{d}\right)$$

With q_0 the momentum of the far field illumination and q the in-plane momentum of the field generated by the dipole.
In the case of $\mathbf{r}$ and $\mathbf{d}$ along the z-axis, we can simplify the formula to the following:

$$E(r) = \frac{e^{iq_0 r}}{r^3}\left((3 - 3iq_0 r - q_0^2 r^2)d - (1 - iq_0 r - q_0^2 r^2)d\right)$$

$$= \frac{2e^{iq_0 r}}{r^3}(1 - iq_0 r) \cdot d$$

With r being the difference in height between the dipole and the probing point: $r = z_d - z_p$.
The electric field becomes in the near-field limit ($r \ll \lambda_0 \Rightarrow q_0 r \ll 1$)

$$E(r) = \frac{2d}{r^3}$$

And in the far-field limit ($q_0 r \gg 1$):

$$E(r) = -iq_0 r \cdot \frac{2e^{iq_0 r}}{r^3} \cdot d$$

If we come back to a general position in space, we have the following relation:

$$q_0^2 = k_x^2 + k_y^2 + k_z^2 \Longleftrightarrow k_z = \sqrt{q_0^2 - k_x^2 - k_y^2}$$

With k being the momentum of the field created by the dipole.
We can switch the in plan momenta k_x and k_y to radial coordinates:

$$k_x = q \cdot cos(\phi); k_y = q \cdot sin(\phi)$$

This means that for a fixed q_0, k_z is a function of the in-plan momentum q.

$$k_z(q) = \sqrt{q_0^2 - q^2}$$

We can identify two cases:
case 1: $q < q_0 \iff k_z$ is real. We have a propagating wave in the z-direction.
case 2: $q > q_0 \iff k_z$ is imaginary. We have an evanescent wave in the z-direction.

Acknowledgements

I would like to thank the following people as this thesis would not have been possible on my own.
I would first like to thank my supervisor, Alexey Kuzmenko, for giving me the opportunity to join his group as a PhD student. I'm proud to be part of his team as the program reffit he developed is a great example of scientific collaboration not being bound by country borders. His curiosity and high modelling capacity will surely advance our comprehension of the Snom signal.
A lot of thanks to Weiwei Luo, who taught me how to use the snom and later collaborated with us from across the globe.
A big thanks to Javier del Valle. The main subject of this thesis comes from a collaboration directed by him. He led this collaboration with clarity, transparency and positivity. It was a pleasure to be part of his project.
I would like to thank colleagues and friends: Giuliano Luigi Esposito, Javier Taboada Gutierrez, Gabriel Giardina and Loïc Musy. Scientific discussions with them were effortless, fun and useful.

I want to thank Jérémie Teyssier who lent his expertise on many machines. Losing him would lead to a lot of lab rooms becoming ghost towns. Iaroslav Gaponenko, in a short time, delivered practical advice that saved me a lot of time. His vision of problems as amusing challenges is refreshing. I have to thank, Willem Rischau, Sylvain Heinzen, Lionel Windels and Daniel Chablais for their help in the making of an electro-magnet. They all needed to be and were very patient as I lack a practical sense.
Pierre Bouillot kindly helped with program installation and computer problems to the point of almost making blue screen fun.
Thanks to Fabienne Hartmeier, Dragana Pantelic and Christophe Schwarz. I was sad each time I came to them with a boring administrative task and was each time greeted with a smile.
Finally, I wish to thank my mother, Yvonne Bercher, who accompanied me through this thesis. Our exchanges were both motivating and refreshing.

Bibliography

[1] A. Hampel, "Interplay between structural, electronic, and magnetic properties in rare-earth nickelates", en, Doctoral Thesis (ETH Zurich, Zurich, 2019).

[2] S. Catalano et al., "Rare-earth nickelates $R\mathrm{NIO}_3$: thin films and heterostructures", Reports on Progress in Physics **81**, 046501 (2018).

[3] J. Torrance et al., "Systematic study of insulator-metal transitions in perovskites $\mathrm{RNiO3}_3$(R=Pr, Nd, Sm, Eu) due to closing of charge-transfer gap", Physical Review B **45**, 8209–8212 (1992).

[4] T. Luibrand et al., "Characteristic length scales of the electrically induced insulator-to-metal transition", Physical Review Res. **5**, 013108 (2023).

[5] J. A. Alonso et al., "High-temperature structural evolution of $R\mathrm{NIO}_3$(R=Ho,Y,Er,Lu) perovskites: charge disproportionation and electronic localization", Physical Review B **64** (2001).

[6] H. Yang et al., "Structural, electrical, and magnetic properties of bulk $\mathrm{Nd}_{1-x}\mathrm{Sr}_x\mathrm{NiO}_3$ (x = 0–0.3)", Solid State Communications **336**, 114420 (2021).

[7] J. Rodríguez-Carvajal et al., "Neutron-diffraction study of the magnetic and orbital ordering in $^{154}\mathrm{SmNiO}_3$ and $^{154}\mathrm{EuNiO}_3$", Physical Review B **57**, 456–464 (1998).

[8] J. L. García-Muñoz, J. Rodríguez-Carvajal, and P. Lacorre, "Neutron-diffraction study of the magnetic ordering in the insulating regime of the perovskites $R\mathrm{NiO}_3$(N=Pr and Nd)", Physical Review B **50**, 978–992 (1994).

[9] H. Park, A. J. Millis, and C. A. Marianetti, "Site-selective mott transition in rare-earth-element nickelates", Physical Review Letters **109** (2012).

[10] C. D. Ordonez, "Electronic coupling in nickelate-based superlattices", en, PhD thesis (University of Geneva, 2021).

[11] S. Johnston et al., "Charge disproportionation without charge transfer in the rare-earth-element nickelates as a possible mechanism for the metal-insulator transition", Physical Review Letters **112** (2014).

[12] M. L. Medarde, "Structural, magnetic and electronic properties of perovskites (r = rare earth)", Journal of Physics: Condensed Matter **9**, 1679–1707 (1997).

[13] G. Catalan, "Progress in perovskite nickelate research", Phase Transitions **81**, 729–749 (2008).

[14] S. Catalano et al., "Electronic transitions in strained $SmNiO_3$ thin films", APL Materials **2**, 116110 (2014).

[15] D. Lee et al., "Sharpened VO_2 phase transition via controlled release of epitaxial strain", Nano Letters **17**, 5614–5619 (2017).

[16] X. Obradors et al., "Pressure dependence of the metal-insulator transition in the charge-transfer oxides $R\mathrm{NiO}_3(R = \mathrm{Pr,Nd,Nd}_{0.7}\mathrm{La}_{0.3})$", Physical Review B **47**, 12353–12356 (1993).

[17] S. Catalano, "Electronic properties of ndnio3 and smnio3 thin films", en, PhD thesis (2017).

[18] P. Chandra and P. B. Littlewood, "A landau primer for ferroelectrics", in *Physics of ferroelectrics: a modern perspective* (Springer Berlin Heidelberg, Berlin, Heidelberg, 2007), pp. 69–116.

[19] N. Caballero et al., "From bulk descriptions to emergent interfaces: connecting the ginzburg-landau and elastic-line models", Physical Review B **102** (2020).

[20] X. Chen et al., "Modern scattering-type scanning near-field optical microscopy for advanced material research", Advanced Materials **31** (2019).

[21] P. Drude, "Zur elektronentheorie der metalle", Annalen der Physik **306**, 566–613 (1900).

[22] M. Fox, *Optical properties of solids (oxford master series in physics, 3)* (Oxford University Press, 2010).

[23] I. Ardizzone, "An optical study of the physics of the rare earth nickelates", PhD thesis (University of Geneva, 2021).

[24] O. S. Heavens, *Optical properties of thin solid films* (Courier Corporation, 1991).

[25] J. R. Sambles, G. W. Bradbery, and F. Yang, "Optical excitation of surface plasmons: an introduction", Contemporary Physics **32**, 173–183 (1991).

[26] Z. Fei et al., "Edge and surface plasmons in graphene nanoribbons", Nano Letters **15**, 8271–8276 (2015).

[27] A. Y. Nikitin et al., "Real-space mapping of tailored sheet and edge plasmons in graphene nanoresonators", Nature Photonics **10**, 239–243 (2016).

[28] I. R. Hooper and W. L. Barnes, "The basics of plasmonics", in *Modern plasmonics* (Elsevier, 2014), pp. 37–74.

[29] J.-J. Greffet, "Introduction to surface plasmon theory", in *Plasmonics* (Springer Berlin Heidelberg, 2012), pp. 105–148.

[30] Z. Fei et al., "Infrared nanoscopy of dirac plasmons at the graphene–SiO_2 interface", Nano Letters **11**, 4701–4705 (2011).

[31] P. Eaton and P. West, *Atomic Force Microscopy* (Oxford University Press, Mar. 2010).

[32] N. Ocelic, A. Huber, and R. Hillenbrand, "Pseudoheterodyne detection for background-free near-field spectroscopy", Applied Physics Letters **89** (2006).

[33] L. Mester, A. A. Govyadinov, and R. Hillenbrand, "High-fidelity nano-FTIR spectroscopy by on-pixel normalization of signal harmonics", Nanophotonics **11**, 377–390 (2021).

[34] B. H. Lukas Novotny, *Principles of Nano-Optics* (Oxford University Press, July 2006).

[35] *Dyadic green's function*, `https://www.eecs.umich.edu/courses/eecs730/lect/DyadicGF_W09_port.pdf`, Accessed: 2024-08-12.

[36] A. Mancini et al., "Near-field retrieval of the surface phonon polariton dispersion in free-standing silicon carbide thin films", ACS Photonics **9** (2022).

[37] A. J. Hauser et al., "Correlation between stoichiometry, strain, and metal-insulator transitions of ndnio3 films", Applied Physics Letters **106** (2015).

[38] S. Bueble and W. W. Schmahl, "Analysis of chevron twin tiling of $LaAlO_3$", Materials Structure **6** (1999).

[39] S. Bueble et al., "Influence of the ferroelastic twin domain structure on the 100 surface morphology of $LaAlO_3$ htsc substrates", Surface Science **400**, 345–355 (1998).

[40] S. Hyun et al., "Dielectric morphology of twin domains in $LaAlO_3$ observed by a scanning microwave microscope", Japanese Journal of Applied Physics **40**, 6510 (2001).

[41] S. Chen et al., "Real-space nanoimaging of thz polaritons in the topological insulator Bi_2Se_3", Nature Communications **13** (2022).

[42] J. R. Kim et al., "Experimental realization of atomically flat and AlO_2- terminated $LaAlO_3$ (001) substrate surfaces", Physical Review Materials **3** (2019).

[43] G. Mattoni et al., "Striped nanoscale phase separation at the metal–insulator transition of heteroepitaxial nickelates", Nature Communications **7** (2016).

[44] P. A. Vermeulen et al., "Unravelling the domain structures in gete and $LaAlO_3$", Crystal Growth and Design **16**, 5915–5922 (2016).

[45] K. W. Post et al., "Coexisting first- and second-order electronic phase transitions in a correlated oxide", Nature Physics **14**, 1056–1061 (2018).

[46] C. Domínguez et al., "Length scales of interfacial coupling between metal and insulator phases in oxides", Nature Materials **19**, 1182–1187 (2020).

[47] W. Fan et al., "Large kinetic asymmetry in the metal-insulator transition nucleated at localized and extended defects", Physical Review B **83** (2011).

[48] S. Lupi et al., "A microscopic view on the mott transition in chromium-doped V_2O_3", Nature Communications **1** (2010).

[49] A. Zimmers et al., "Role of thermal heating on the voltage induced insulator-metal transition in VO_2", Physical Review Letters **110** (2013).

[50] M. D. Pickett, G. Medeiros-Ribeiro, and R. S. Williams, "A scalable neuristor built with mott memristors", Nature Materials **12**, 114–117 (2012).

[51] M. Ignatov et al., "A memristive spiking neuron with firing rate coding", Frontiers in Neuroscience **9** (2015).

[52] P. Stoliar et al., "A leaky-integrate-and-fire neuron analog realized with a mott insulator", Advanced Functional Materials **27** (2017).

[53] J. del Valle et al., "A caloritronics-based mott neuristor", Scientific Reports **10** (2020).

[54] W. Yi et al., "Biological plausibility and stochasticity in scalable VO_2 active memristor neurons", Nature Communications **9** (2018).

[55] S. M. Bohaichuk et al., "Fast spiking of a mott VO_2-carbon nanotube composite device", (2019).

[56] S. Oh et al., "Energy-efficient mott activation neuron for full-hardware implementation of neural networks", Nature Nanotechnology **16**, 680–687 (2021).

[57] S. Kumar, J. P. Strachan, and R. S. Williams, "Chaotic dynamics in nanoscale NbO_2 mott memristors for analogue computing", Nature **548**, 318–321 (2017).

[58] M. Jerry et al., "Stochastic insulator-to-metal phase transition-based true random number generator", IEEE Electron Device Letters **39**, 139–142 (2018).

[59] J. d. Valle et al., "Generation of tunable stochastic sequences using the insulator–metal transition", Nano Letters **22**, 1251–1256 (2022).

[60] I. Olivares et al., "Optical switching in hybrid VO_2/Si waveguides thermally triggered by lateral microheaters", Optics Express **26**, 12387 (2018).

[61] G. Li et al., "Photo-induced non-volatile VO_2 phase transition for neuromorphic ultraviolet sensors", Nature Communications **13** (2022).

[62] L. D. Sánchez et al., "Experimental demonstration of a tunable transverse electric pass polarizer based on hybrid VO_2/silicon technology", Opt. Lett. **43**, 3650–3653 (2018).

[63] K. J. Miller et al., "Silicon waveguide optical switch with embedded phase change material", Opt. Express **25**, 26527–26536 (2017).

[64] D. Lee et al., "Sharpened VO_2 phase transition via controlled release of epitaxial strain", Nano Letters **17**, 5614–5619 (2017).

[65] P. Stoliar et al., "Universal electric-field-driven resistive transition in narrow-gap mott insulators", Advanced Materials **25**, 3222–3226 (2013).

[66] R. Rocco et al., "Exponential escape rate of filamentary incubation in mott spiking neurons", Physical Review Applied **17** (2022).

[67] W. Schnelle, R. Fischer, and E. Gmelin, "Specific heat capacity and thermal conductivity of $NdGaO_3$ and $LaAlO_3$ single crystals at low temperatures", Journal of Physics D: Applied Physics **34**, 846–851 (2001).

[68] P. Salev et al., "Transverse barrier formation by electrical triggering of a metal-to-insulator transition", Nature Communications **12** (2021).

[69] J. D. Jackson, *Classical electrodynamics (third edition)* (Wiley, 1999).